Lynx Motorsports Senior Design Expo Report

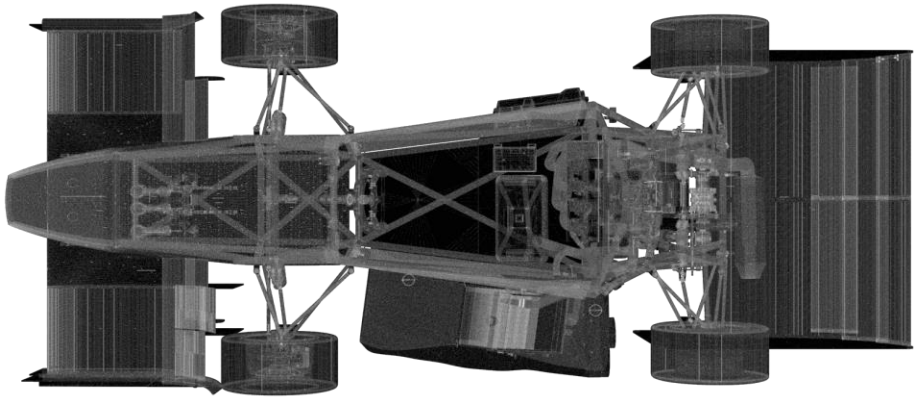

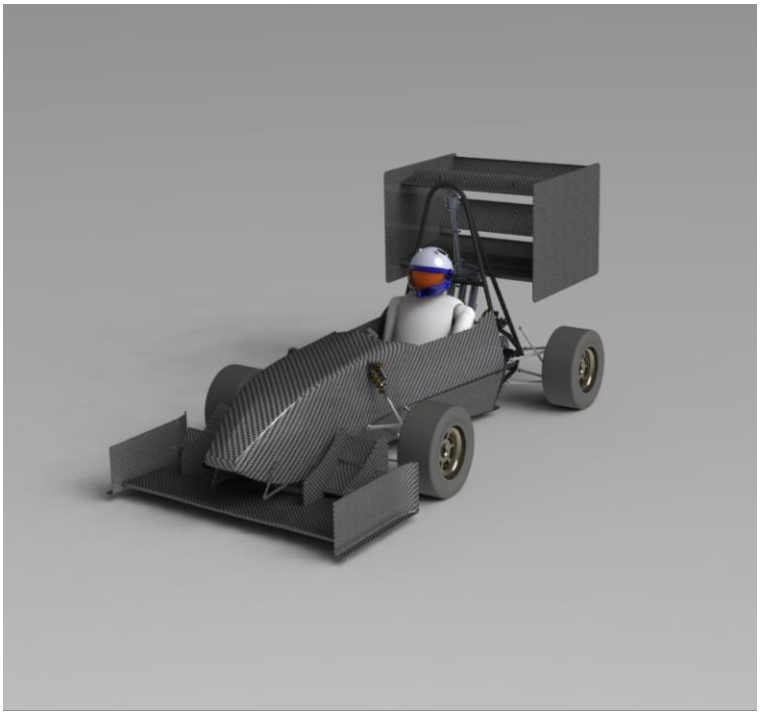

Authors:

Nick Lanzoni

Donald Robb

Hunter Blevins

Daniel Ledvinka

Jared Hardinger

Joseph Valdez

Robert Sellers

Adam Sulima

Ben Larson

Christopher Geist

Erik Druva

Kevin Cross

Nick Sirois

Abstract

Formula SAE is an internationally recognized engineering design competition open to undergraduate and graduate students where students design, manufacture, and test an open-wheeled formula style race car. This document covers the objectives of the 2020 Lynx Motorsports team and the design and manufacturing decisions that were made to achieve them.

Table of Contents

List of Tables

List of Figures

Team 2020 Objectives

1. Decrease overall car weight by 10%
2. Decrease wheel diameter from 13inch to 10inch
3. Finish Top 2020 at FSAE West
4. Be the best team from Colorado

Suspension

Tires and Wheels

The first and most important design consideration for the 2019-2020 FSAE season was our choice of tire. In previous years, the team had used the Hoosier 20.0 x 7.0-13 R25B tire, which weighed 12 lbs, and costs $182 per tire. Over the summer the team spent time analyzing what tire the best teams from around the world use and found that most of the top 25 teams in the world use the Hoosier 16.0 x 7.5-10 LC0. After realizing this, data from the FSAE tire Test Consortium and the OptimumT software was used to discover why so many good teams used this tire. So many teams use the 10" LC0 because it is the superior tire choice for three reasons, weight, lateral grip, and cost.

The 10" LC0 is 2 lbs lighter than the 13" R25B (16% lighter). Additionally, because the LC0 has a smaller outside diameter it has a lower polar
moment of inertia meaning that less energy is wasted rotating it and as a driver the car would be able to respond to steering input more quickly, which is extremely necessary on a twisty autoX track.

The second major reason that the 10" LC0 is superior to the 13" R25B is that it has more lateral grip. Figure 1 below shows the 10" tire in pink and 13" in blue. By examining the lateral force against tire slip angle it is clear that for each degree increase in slip angle the 10" tire is able to generate more lateral force than the 13" tire at the same amount of vertical load. Meaning that the LC0 would continue to provide traction during a corner after the R25B had begun to slide, thus allowing the car to corner at a higher G than when using 13" tires.

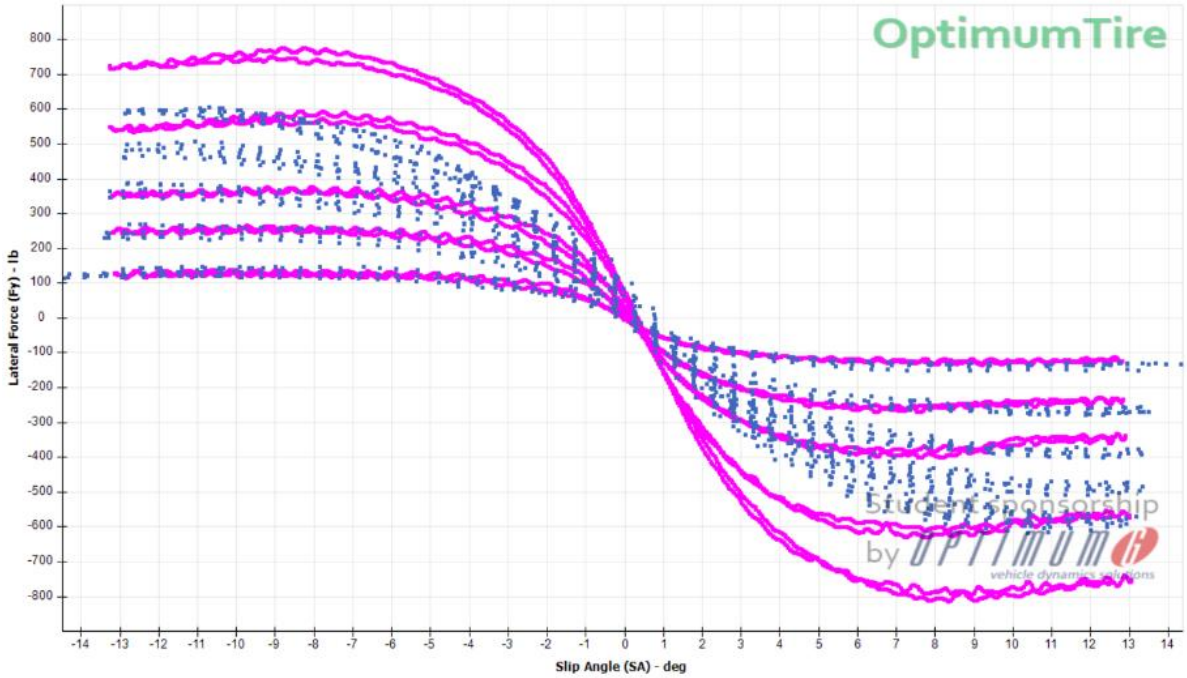

Figure 1: *Slip angle vs Lateral Force comparing 10in LC0 (pink) and 13in R25B (Blue)*

The third reason that the 10" LC0 is superior to the 13" R25B is a simple one, cost. The 10" LC0 costs $159 per slick tire. Generally, the team orders 10 slick tires and 5 rain tires every year. By switching from the 13" tire to 10" the team will save $407 on tire cost this year.

After it became clear why the 10" tire was the preferred choice of the top team's further analysis was done in order to determine the tread width, size, and rubber compound. Hoosier offers 10" diameter tires with 6.0", 6.5", and 7.0" tread widths. By comparing the 6.0" rim shown in Figure 4 as pink against the 7" rim width shown as blue, it was evident that the 7.0" width was preferable. Which logically makes sense, a wider tire will have a larger contact patch and therefore be able to supply the car with more lateral grip when compared to a thinner tire. This is the same reason why F1 cars have moved away from the skinny tires of the 1950's and 1960's and now use wider tires.

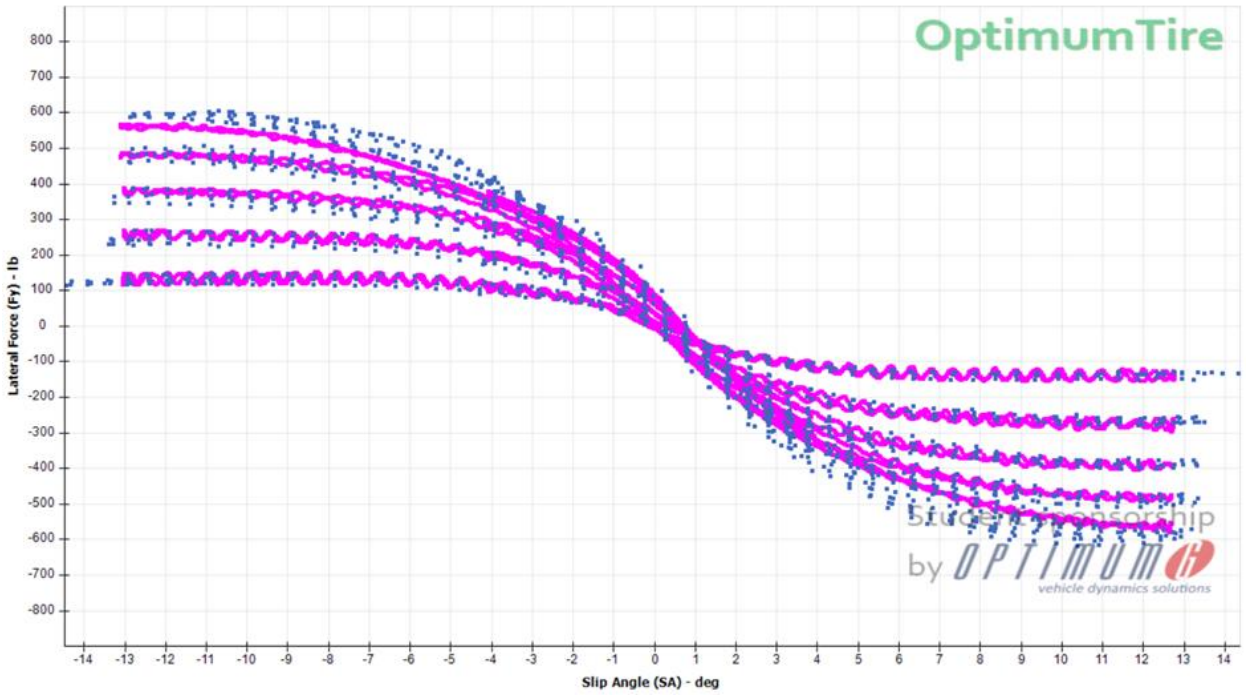

Figure 2: *Slip angle vs Lateral Force comparing tire tread width 7.5in LC0 (Blue) and 6in LC0 (Pink)*

After the thread width was selected the choice the R25B and LC0 compounds needed to be made. The same graph of slip angle against lateral force was made to compare the two compounds that Hoosier manufacturers. This graph is shown below as Figure 3 displays the 10" LC0 in pink and the 10" R25B in blue.

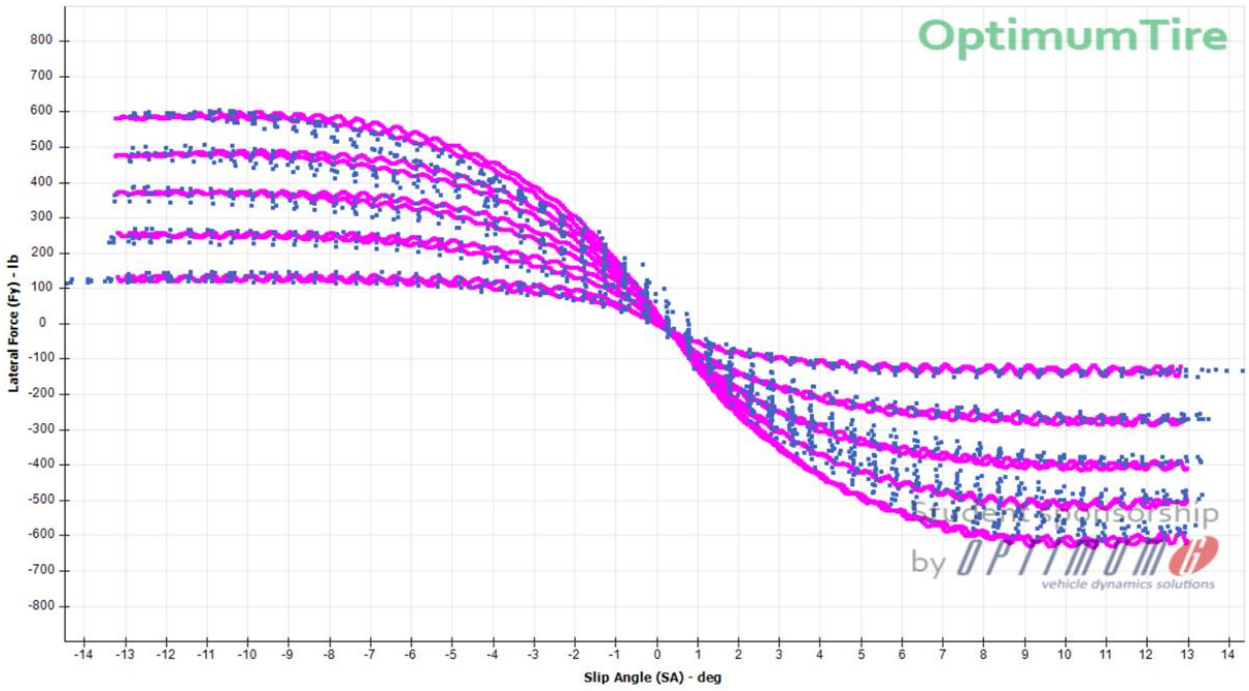

Figure 3: *Slip angle vs Lateral Force comparing 10in LC0 (pink) and 10in R25B (Blue)*

Compared to the previous plots shown, these two tires perform very closely but if you take a closer look at the lateral force at lower slip angles (-5 to 5) you will see that the LC0 has a slight edge over the R25B.

After the different tire Hoosier tire variants had been compared, it was clear that the 10.0 x 7.5 LC0 is the superior tire available for our 2019-2020 car.

It is also important to mention that this choice was constrained by the limitations of the Tire Test Consortium. Most tire data is not publicly available and therefore it is very difficult to compare tires that the Test Consortium has not tested, and therefore my analysis was limited to those tires that the Consortium had already analyzed and no additional tires were considered. If in the future, the team would like to change tire compounds they might spend time looking outside of compounds tested by the Consortium. Two teams, University of Akron, and Delft University of Technology use tires that have not been tested by the consortium and it could be a good use of time to figure out why.

Because the tires are the most important factor in suspension characteristics several more studies we done in order to determine basic characteristics of the tire. These include cornering stiffness, temperature sensitivity, optimum camber settings, and optimum tire pressure.

To calculate cornering stiffness and spring rate of the tire which are necessary when determining the diameter and drop links of the anti-roll bar the 150,000 data points from the testing consortium were filtered down to 2000 by establishing several constants. These were 0 degrees camber, 175 lbs of normal load on the tire, 45 mph (estimated average car speed during AutoX) and 12 psi of pressure. By eliminating all data that did not fit these conditions I was able to condense the mass of data into a manageable size. From there it was easy to calculate a cornering stiffness of the LC0 at 315 N/deg. This value was then compared with the cornering stiffness of the tire using the same conditions except at 8 psi of tire pressure. The average stiffness was almost identical. This means that as we test and tune the car later this year we should not rely on being able to change tire pressure in order to induce or reduce oversteer, and that the adjustments of the anti-roll bar and dampers will be much more important.

Finally, the LC0 tire model was fit to Pacejka's (magic) tire model, which characterizes a tire using 10-20 different coefficients in order to predict the tires behavior at any given value of vertical load. This model will not be very important for this year's car but has been instrumental in my initial lap time simulation software that will need to be continuously developed. The current simulation script uses the Pacejka tire model to predict all the lateral loads and once the lateral load is calculated, tire cornering stiffness, and spring rates can be found very easily.

The eventual goal with the tire model is to be able to predict when and where on the track the car is likely to lose traction, which would allow us to predict a lap time. In professional motorsport, performance engineers can examine the tire data and sensor data and tell the driver in which corners he is underperforming or leaving time on the table. We are currently miles

away from this level of precision, but we are slowly making steps in an effort to reach it. At this stage the software is able to predict with reasonable accuracy a single skidpad lap. Skidpad is a perfect choice as a first simulation step because it is a single turn of constant radius which allows me to predict the car much more easily than say trying to predict AutoX which has 20+ corners each of a different radius

Kinematics

With the change in tires already being made, the entire kinematics of the car needed to be redone. One of the things that we noticed at competition was that we had trouble navigating low speed turns at competition and we were determined to make sure that our car this year would not struggle to make the hairpin turns. In the summer of this year we checked the course maps for both the endurance and autoX events at competition shown as Figure 4 and Figure 5 respectively, and characterized each turn as either high speed, middle speed, or slow speed and found that 75% of all turns are either slow speed or middle speed turns. Meaning that your car's ability to navigate slower speed turns is the defining measure of how quick your car is around the track.

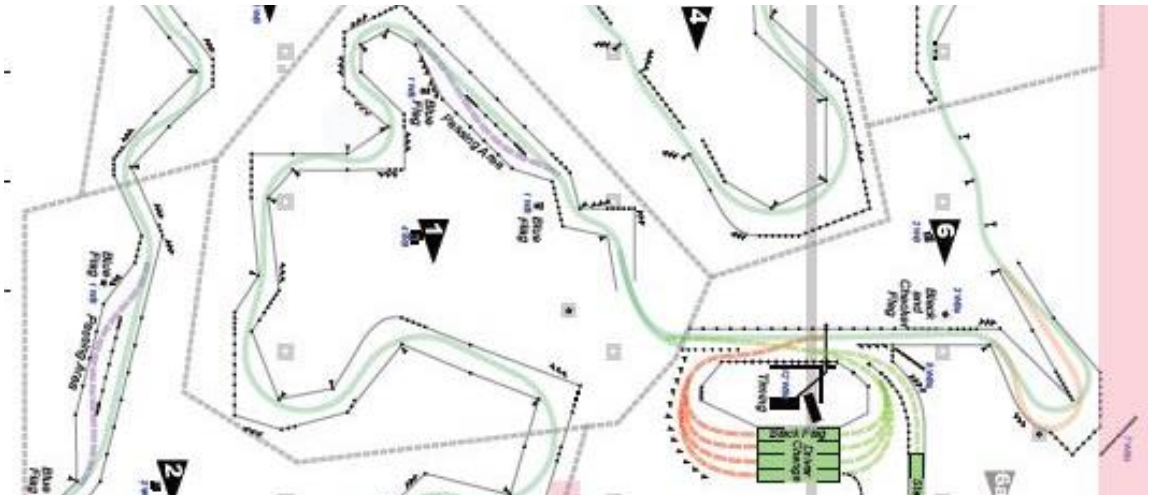

Figure 4: *2019 FSAE Lincoln Endurance Layout*

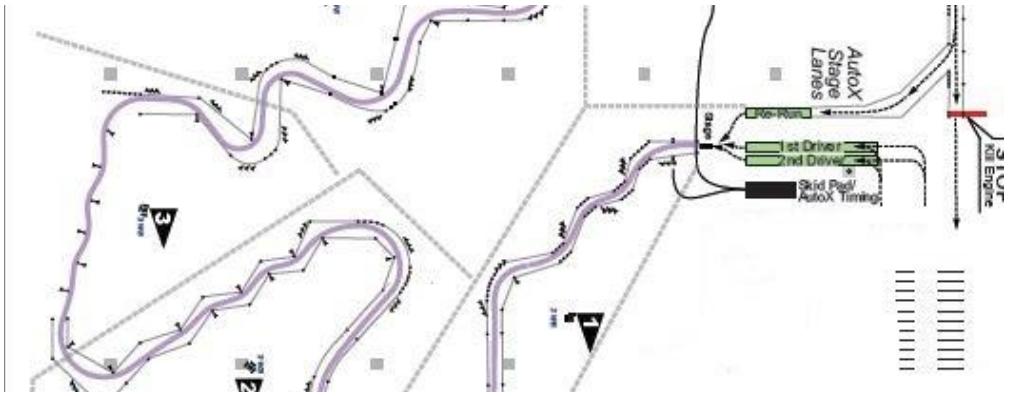

Figure 5: *2019 FSAE Lincoln AutoX Layout*

With the intention of increasing performance in slow speed corners at the top of the priority list, the first part of the kinematics that was considered was the overall dimensions, front track width, rear track width, and wheelbase. Shown below in Figures 6 and 7

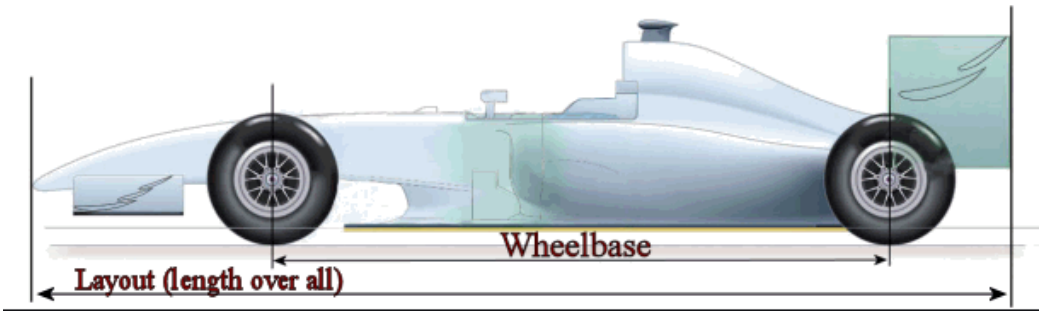

Figure 6: *Example of Vehicle Wheelbase dimension*

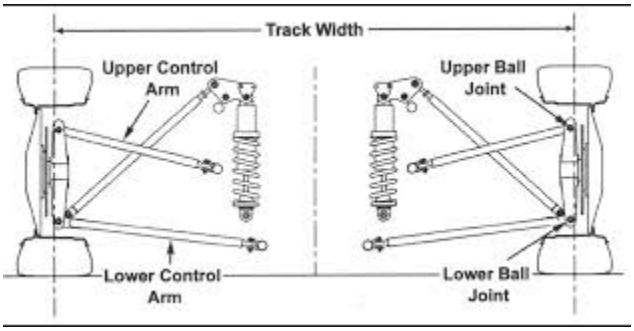

Figure 7: *Example of Vehicle track width dimension*

After averaging the top teams in the world, it was found that they had an average wheelbase of 1554mm and the LX-18 had a wheelbase of 1650mm. This year a wheelbase of 1550mm was

chosen which is the shortest possible wheelbase that still allows the chassis to accommodate the Honda CBR 600 engine and a 6'2" driver.

To determine the Front and Rear track width a free body diagram was used to determine the track width that we would need to not roll over during a 2g turn. Because there are roughly two slalom sections per autoX and endurance track it is advantageous to keep your track width as narrow as possible while still having some margin for rolling over during cornering.

The next significant step of the kinematic design was to set the pickup points on the chassis which were heavily constrained by the packaging of the engine and the pickup points on the upright which needed to be packaged around the new wheels. When setting the pickup points the most important thing to examine is how the location of the roll center changed with the relative amount of active camber. As you make your roll center lower, which would decrease weight transfer during cornering, you also decrease the amount that your wheel moves during roll. This phenomenon is shown in Figure 8 below.

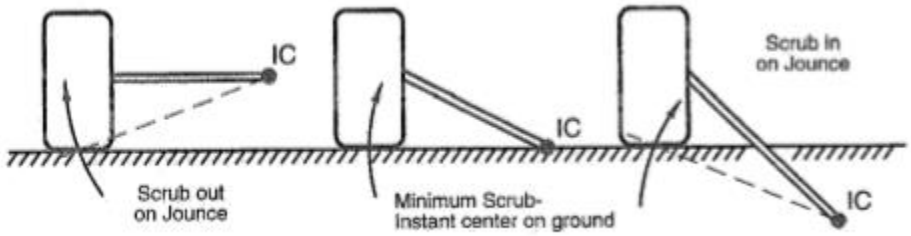

Figure 8: *Diagram of how changing your instantaneous roll center changes the active camber of the tire*

The compromise that was decided on was because the rear suspension was so heavily constrained by packaging that we would use the best packaging option and work around the roll centers. After running several optimumK simulations it was found that the rear suspension had a roll center of 2.5in above the ground plane, and for every degree of body roll the tire had 0.5 degrees of camber change. We were then able to move the front pickup points around to closely match the rear roll center. One of the problems that we saw on last year's car was mid-corner

understeer, and after extensive research one of the easiest ways to fix that was to set your roll centers to very close to the same height or to even set the rear roll center slightly higher. Because we were able to completely design the front chassis around the suspension, we were able to dial in the front roll center to be 0.25in lower that the rear suspension. By doing this we hope to fix the mid-corner understeer and increase corner exit performance. A chart showing the comparison between rear and front roll centers during roll is shown below as Figure 9

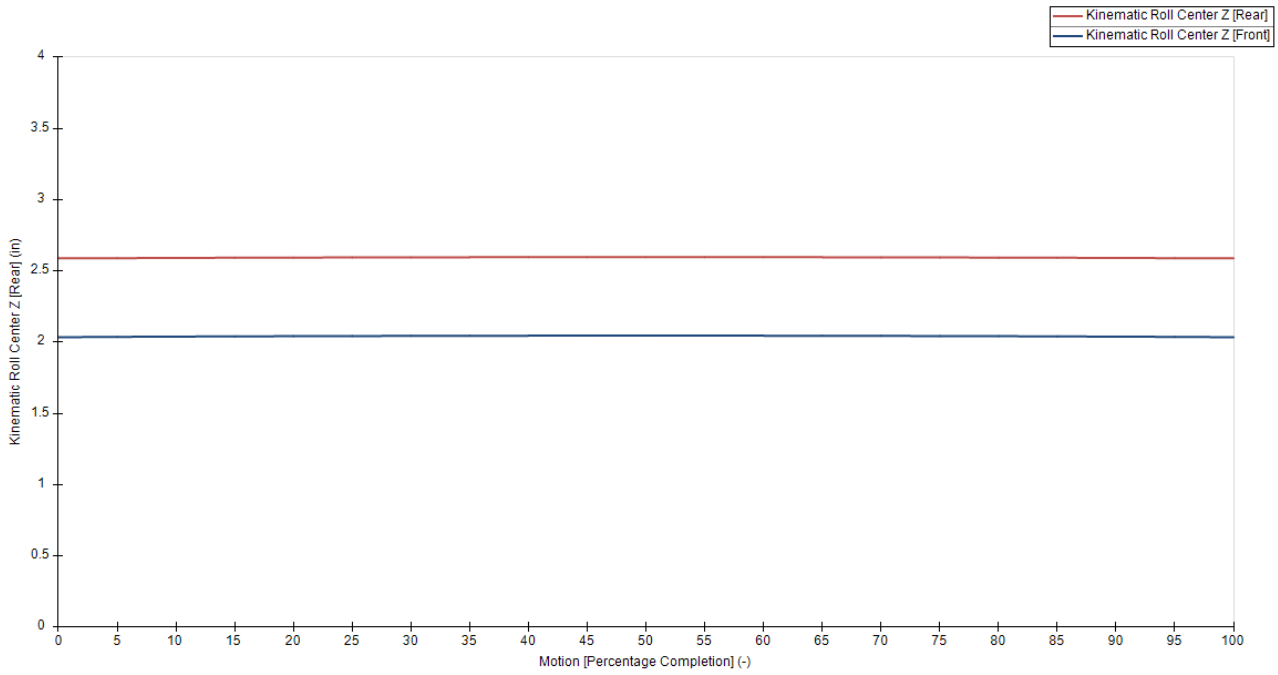

Figure 9: *Roll Center Vertical Movement during Cornering Situation*

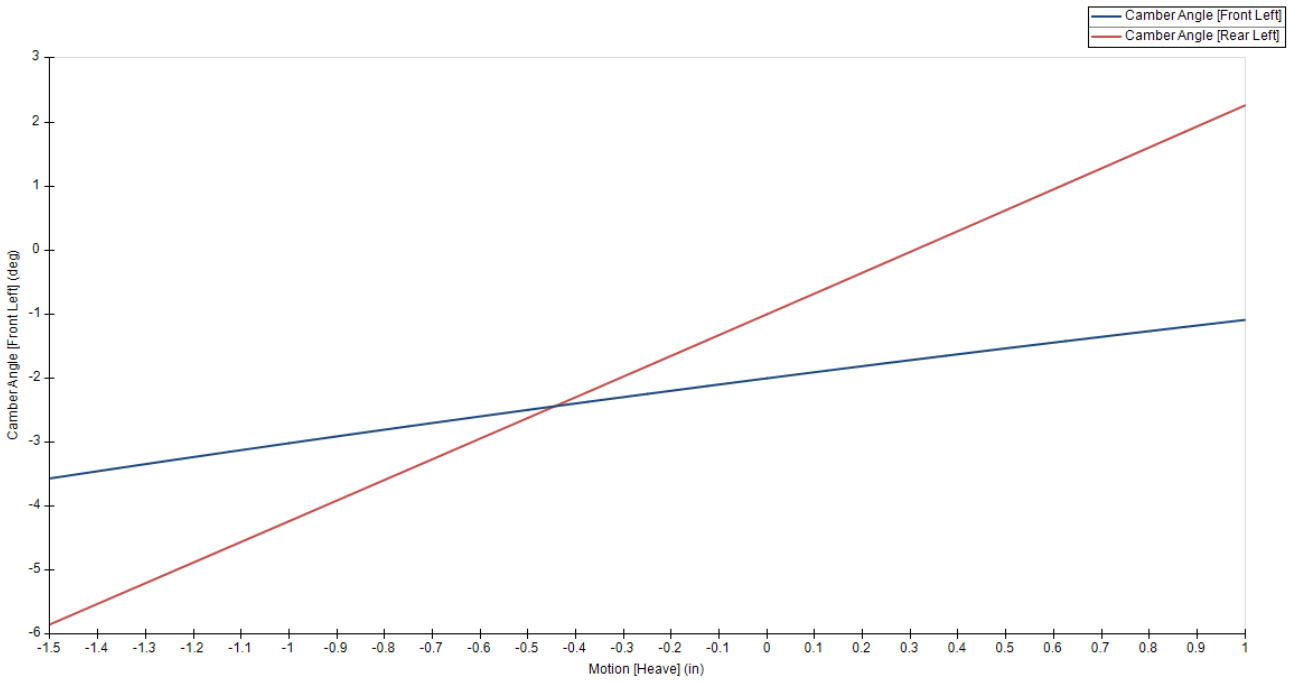

Figure 10: *Vehicle active camber during a pure chassis roll movement*

The next step of the kinematics is the motion ratios of the front and rear are identical. In the front we decided that as a measure to drop weight and manufacturing time, the front suspension would be direct actuation, meaning that the motion ratio would be close to fixed. After simulating the front suspension, we were then able to adjust the rear bell crank geometry in order to match the motion ratio of the front suspension. The Figure 11 shown below demonstrates the spring length change in pure heave. The motion ratio is calculated by finding the slope of these linear lines.

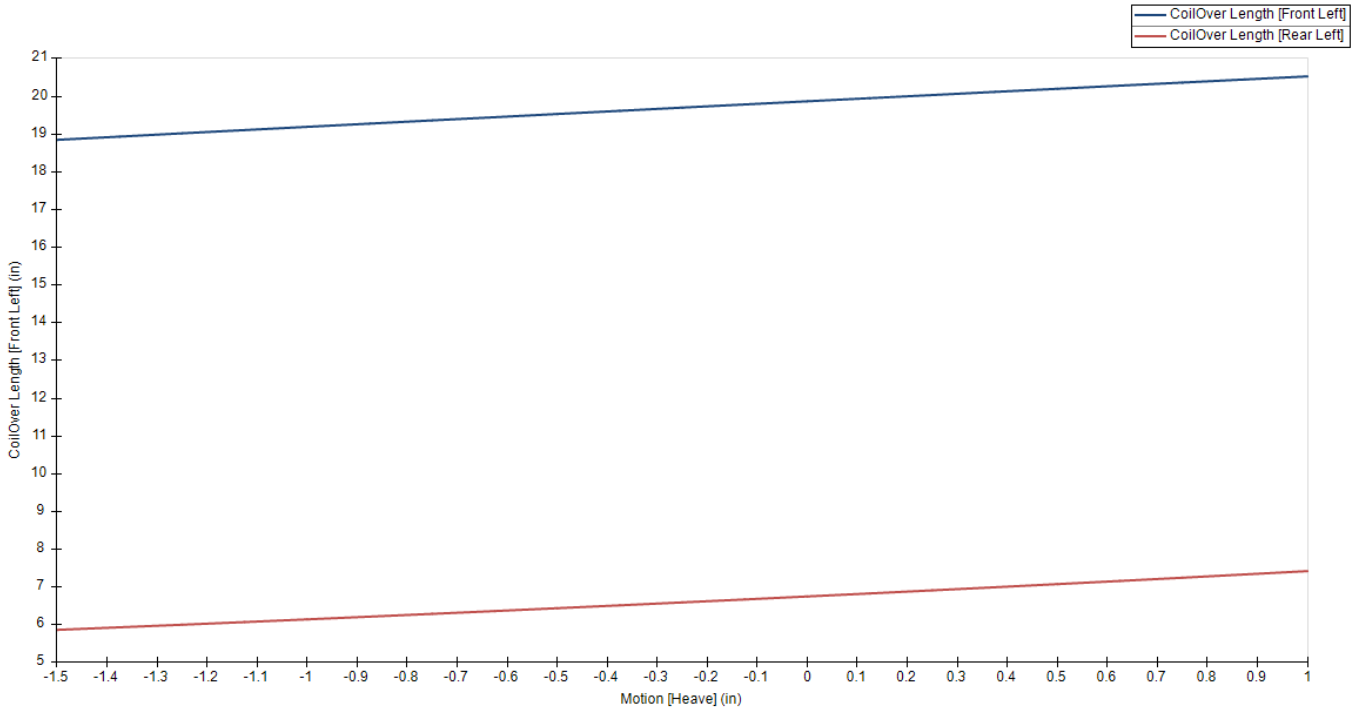

Figure 11: *Front and Rear Motion ratio Comparison during Heave*

Once the roll centers and pickup points are set, the only remaining task is making sure that the tires are not moving in unexpected directions when the car is cornering. By using optimumK to create various motion studies to simulate the chassis movement during cornering. Plots for these simulations are shown below.

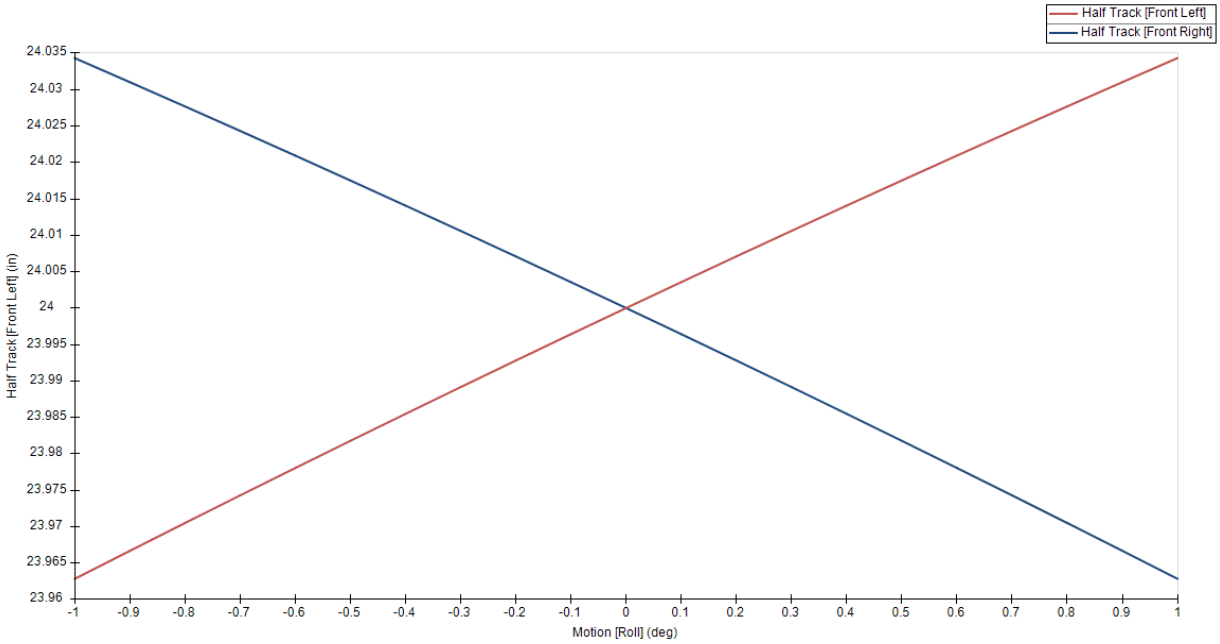

Figure 12: *Vehicle Track Width during Roll Movement*

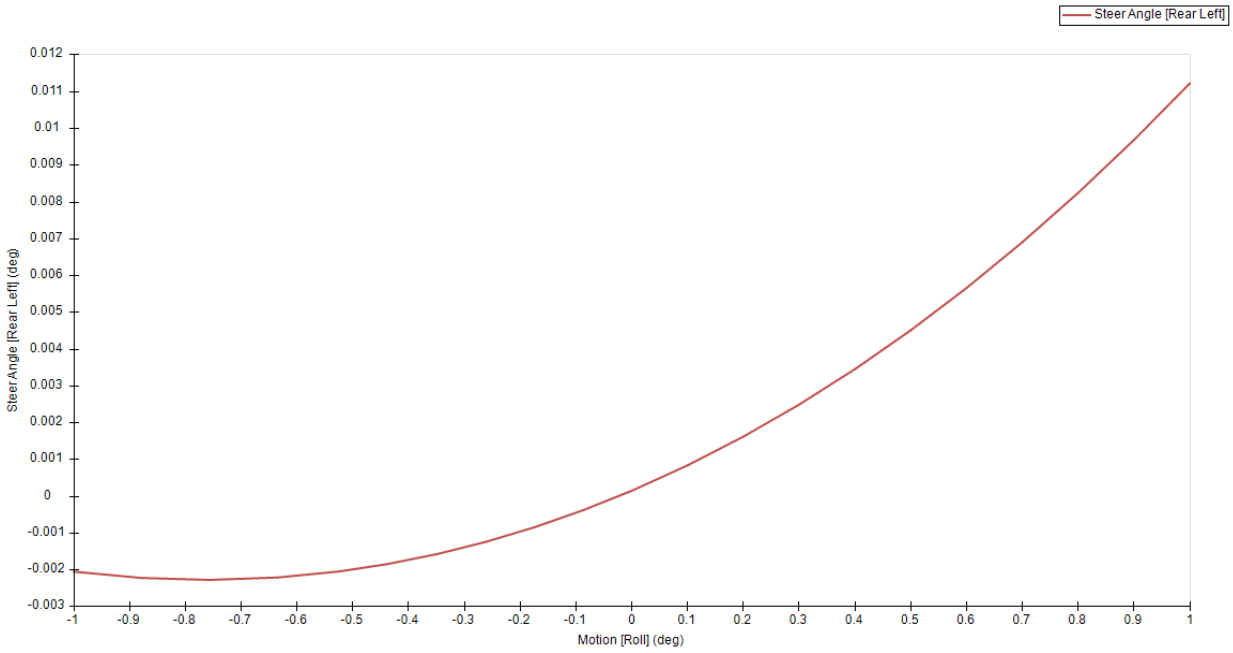

Figure 13: *Rear Steer angle change in Chassis Roll Movement*

Hubs

The hubs are where the wheels attach to the vehicle. Via two bearings, the hubs spin freely within the uprights allowing the wheels to spin while the car is in motion. The rear hubs must also transmit the driving torques from the drivetrain, and all four hubs must be able to directly take braking torques. The wheels, uprights, and brakes attach directly to the hubs. Design considerations for the hubs were based on the adjustments needed to accommodate the change to 10-inch diameter wheels. The change was done to assist in the car-wide weight loss goals.

In an effort to improve weight loss, the hubs will be made of Aluminum 7075-T6 and will be hollowed out wherever possible. The aluminum along the threads will be anodized to help the parts longevity with the wheels being taken on and off over time.

The current part models have bore sizes chosen to minimize weight, while still being machinable and able to handle threads being cut into the ends. On the rear hubs, the bore cannot go all the way through because the "back" of the hub, or the non-wheel holding side, needs to be able to transmit the driving torque of the car via a constant velocity joint. The wheel sides will be threaded with seven standard 3 mm pitch threads on the 50 mm OD. Five threads is more than enough holding force, and allows for the nut that will mate with it to be machinable and convenient for taking on and off. Equation (1) was used for confirmation of the thread holding strength.

$$F_{nut} = \pi D[0.75 * (number\ of\ threads\ needed)] * [0.58 * (F_{yield,Al\ 7075-T6})]$$

This calculation confirmed that due to the material properties of Aluminum 7075, one thread would mathematically be sufficient to hold the maximum forces the threads will feel. This is unrealistic due to how thin this nut would be.

Current part models:

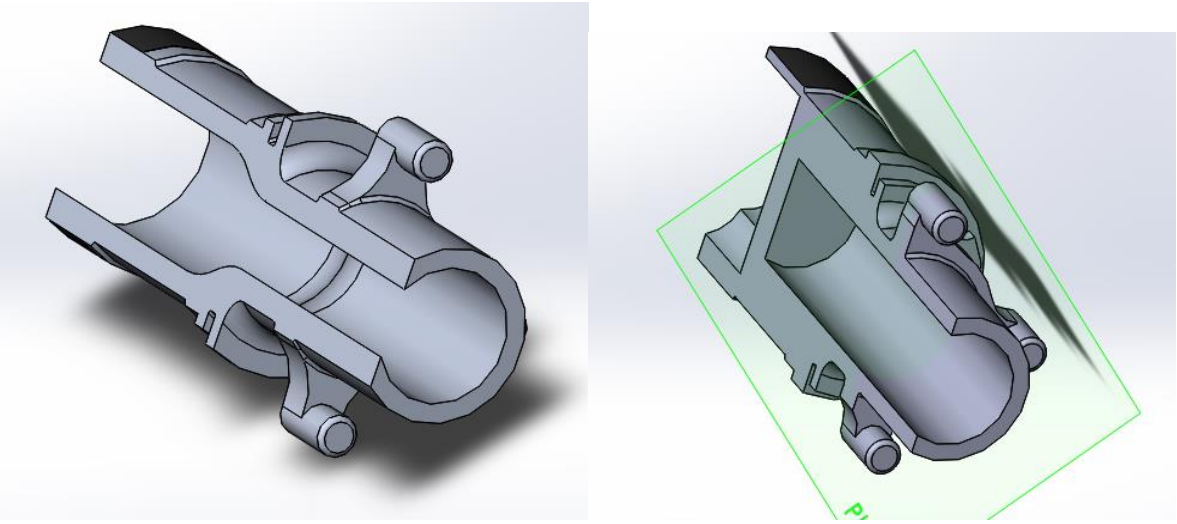

Figure 14: *Cutaway Views of the current Front (left) and Rear (Right) Hub Models*

Free Body Diagrams:

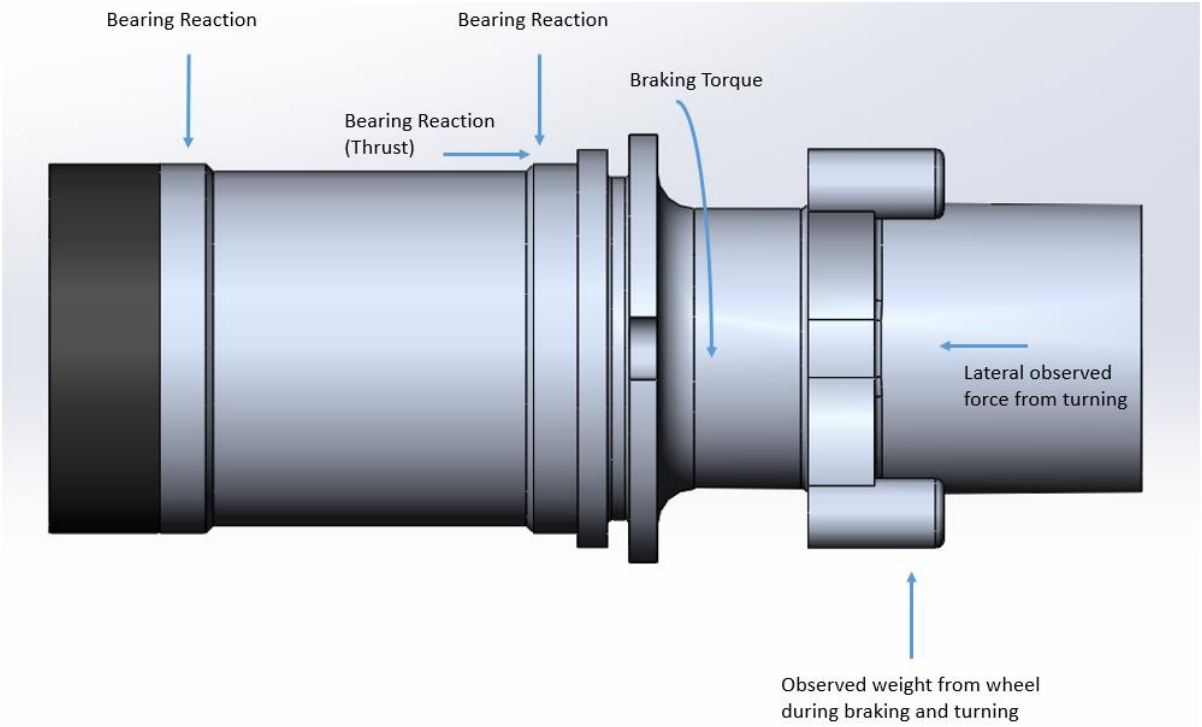

Figure 15: *Free Body Diagram of the maximum forces experienced by the Front Hub*

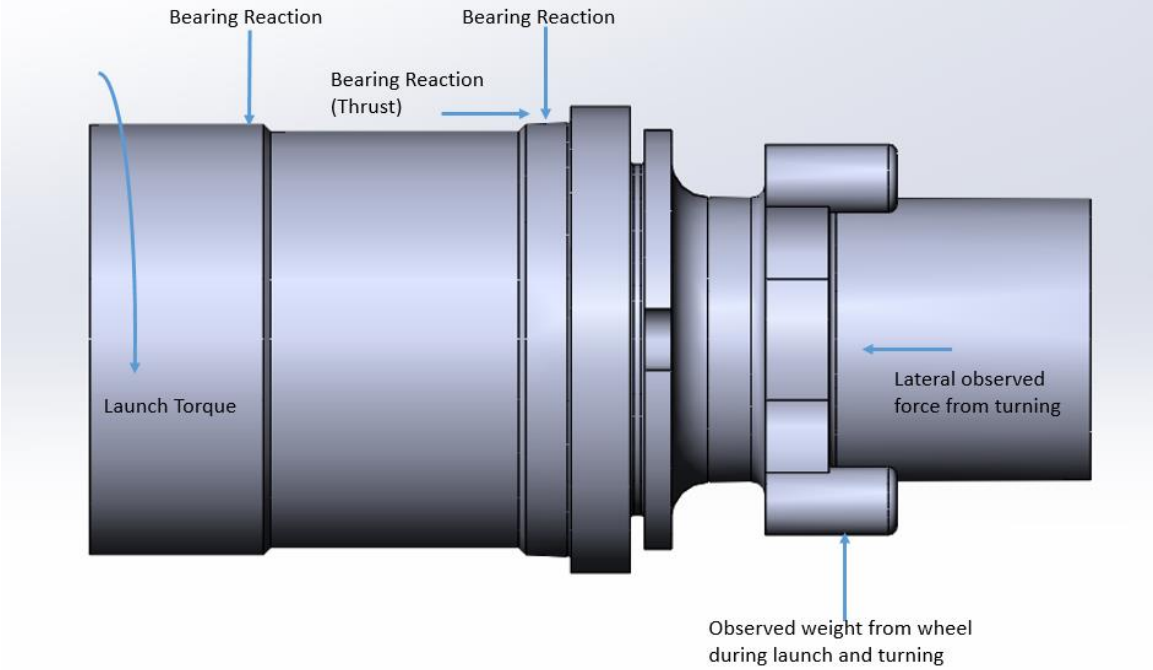

Figure 16: *Free Body Diagram of the maximum forces experienced by the Rear Hub*

The maximum loads felt for the front hubs are during an event of braking, turning, and hitting a bump. During braking, the hub experiences both torque from the brake rotor as well as increased weight of the car from the weight shift. Turning increases the perceived weight of the car at a particular hub, and translates into a lateral force putting the hub in tension. A 2g bump brings the perceived weight of the car to double its static value. The maximum loads for the rear hubs are during a turning, bump, and launch event. Like braking on the front, a launch increases the weight felt on the rear hubs which combined with a 2g bump and turning causes the static value of the car's weight on the hub to increase. During a launch, a torsion is felt on the rear hubs as the constant velocity joint transmits the forces of the drivetrain through the hub to the wheels.

Hub Finite Element Analysis:

Current finite element analysis has the safety factor using standard ASM data for Aluminum 7075-T6. Both the front and rear hubs with bore sizes as is have safety factors in the range of 1.3 in isolated locations, and well over 5 for the rest of the parts.

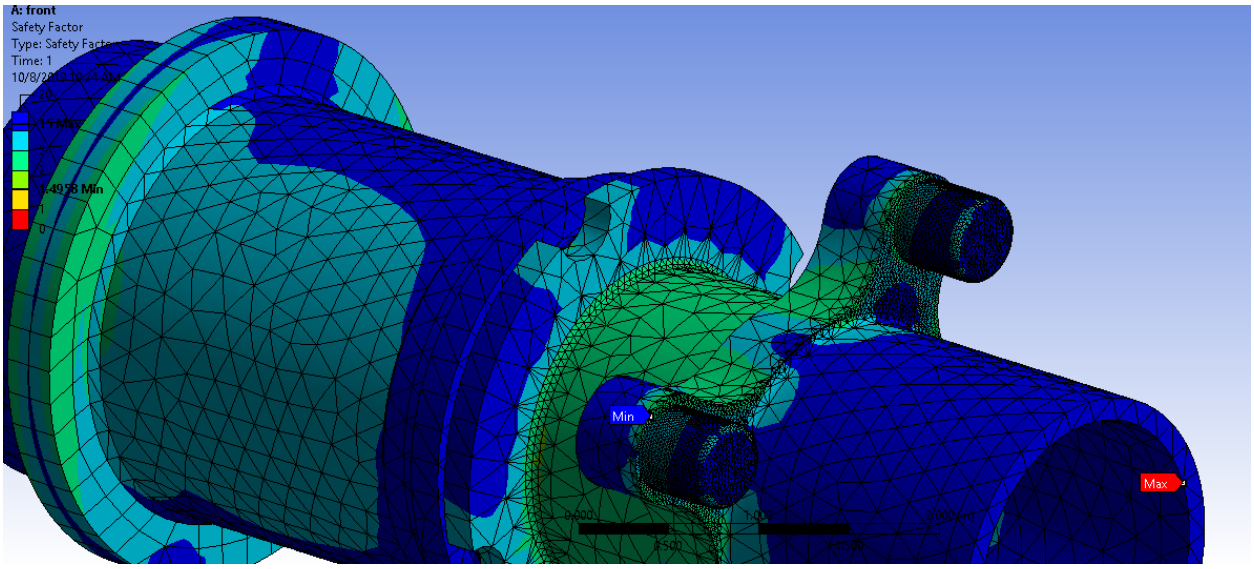

Figure 17: *Finite Element Analysis of the Front Hub Under Maximum loading conditions*

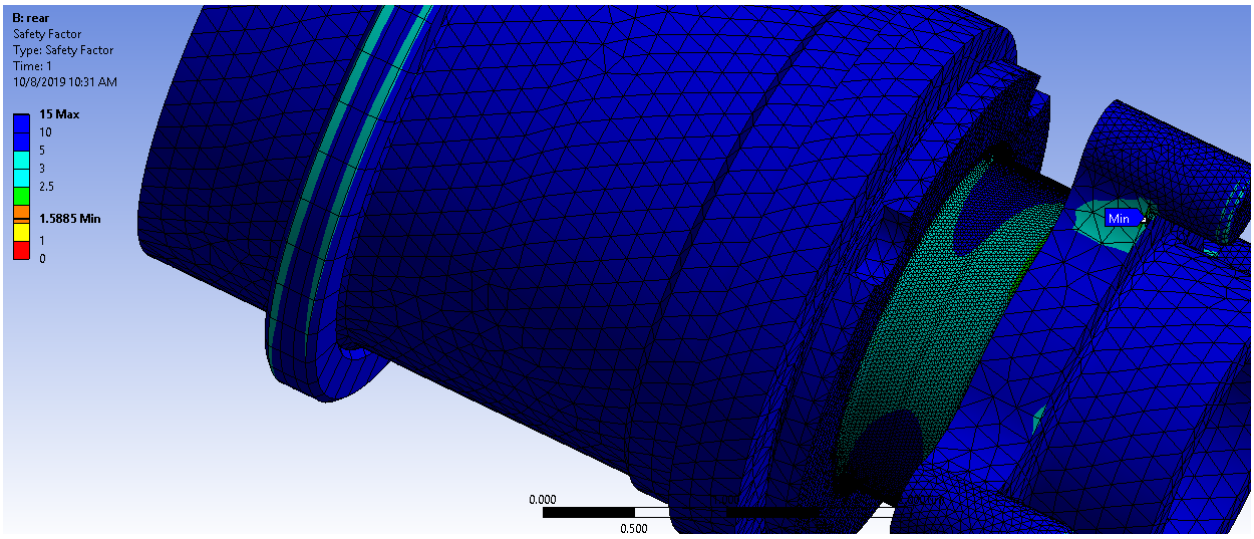

Figure 18: *Finite Element Analysis of the Rear Hub under Maximum loading conditions*

Machining began on the hubs in November. The first front hub was finished on January 27th, with the second one completed on the 29th after adjusting the machine process for both to

include an additional lathe set-up. The rear hubs were completed on February 21st and 24th respectively.

Challenges included holding bearing size tolerances, keeping tools from deflecting too much, and most notably assuring all operations allowed the part to remain concentric with all previous operations. For the case of holding concentricity, the parts were re-indicated before each cutting operation.

The hubs require 8 nuts, one on each side of each hub, to hold them and the wheels in place while in service. In order for the nuts that hold on the wheels to survive being put on and taken off repeatedly, it was decided to make them out of stainless steel. This was chosen not just because of stainless being ductile and more able to take impacts, but also because repeated wear between two aluminum parts would be more likely to gall. Galling of the wheel nuts and wheel hubs could permanently disable both. Four of these nuts have been made, with two being of acceptable quality at this time. These four will be usable to reach our first drive goals, but more will be made for higher quality and to have spares.

The four nuts on the back of the hubs are currently being redesigned to accommodate the speed sensors on each wheel. These nuts will be made of aluminum due to the fact that they will just be installed once. Design is nearly complete, and machining will begin as soon as possible to attempt to meet our first drive goals.

The eight nuts necessary for the hubs have also been designed with the required minor diameters for the various thread sizes. Some of the diameters were adjusted for anodizing as well. 4 of the nuts are all of matching sizes to hold on the wheels. The other 4 go on the backs of the hubs to keep it attached once installed and are sized accordingly.

Figure 19: *Inside view of hub and wheel fit*

Uprights

The uprights are the main connection between the tires and the main body of the car. They are involved in the steering (in the front), house the bearings and hubs, transfer braking and turning forces from the tires to the car, and provide stability during turning. Using a pair of bearings, the hubs rotate freely inside the center of the uprights. There are mounting points at the top and bottom of the uprights that attach to the upper and lower A-arms. This is the main support holding the car above the ground. There will be a steering clevis connecting the uprights

to the tie rods which will control the car's steering. The uprights this year will be a complete redesign from the 2018-2019 car both because of the change in wheel size from 13 inches to 10 inches and the fact that last year's uprights were much too flexible. Initial analysis indicates that this new design will be three times as stiff while also being much lighter.

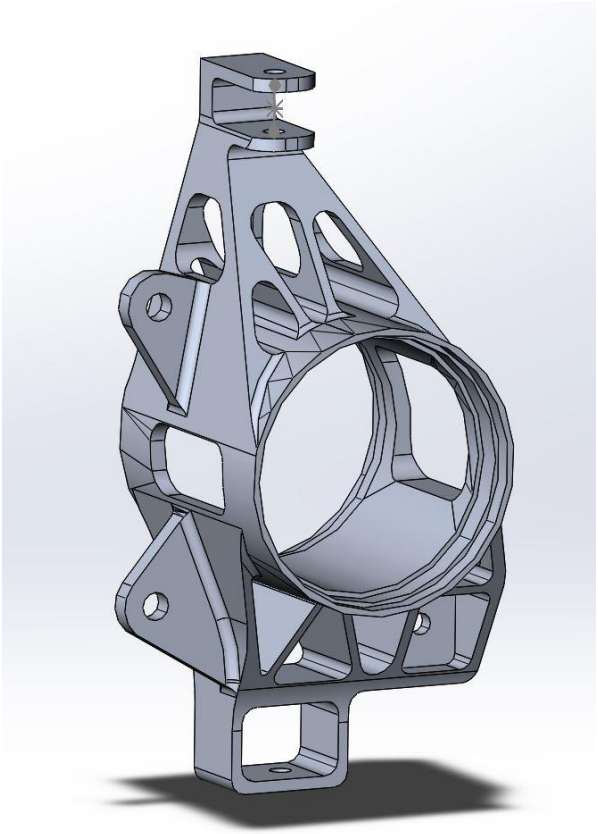

Figure 20: *The front right upright*

When designing the uprights, the main goal is to provide the maximum amount of stiffness while also remaining lightweight. The stiffness is important because deflections provide unpredictable feedback to the driver during turns. A total failure of the part, such as if the uprights are unable to survive the braking forces, will result in an inoperable car. The uprights will be manufactured from Aluminum 7075-T6 to provide maximum strength while remaining

lightweight. In order to increase stability in the uprights, this year's models will be much thicker at the center with a thickness of 3.4 inches, whereas last year's uprights were significantly thinner. To reduce the weight, the thickness will taper down towards the top and bottom while remaining thick enough to survive all forces. Holes will also be cut into the uprights through the front/back direction and in parts of the sides. The bearings will be pressed into place. The upper mount for the A-arm has the clevis built into the upright to eliminate the need to machine a clevis and the use of bolts to mount the extra material. Mounting positions for the A-arms and steering were determined by the kinematics, and the mounting position for the brake calipers were determined by the braking system lead.

The uprights will experience forces at the upper and lower mounts, the brake caliper mounts, the steering clevis mount, and the bearing seats. The forces experiences from the steering clevis will be relatively insignificant. To calculate the largest forces experienced, we took into consideration a situation where the car is braking and turning to the maximum. When braking and turning at full forces, we determined that there will be a 2000 lb braking force directly downward from the brake caliper and a reaction force from the hub and tires with components (-675, 800, 450) lbs. that will be transferred from their respective sources to the upper and lower mounts. These were the forces used in the FEA analysis.

Free Body Diagram:

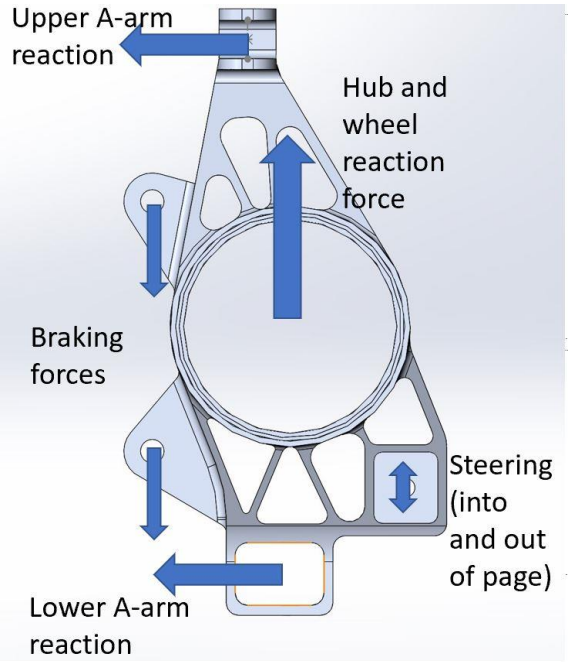

Figure 21: *Free Body Diagram of the maximum forces experienced by the front upright*

FEA analysis

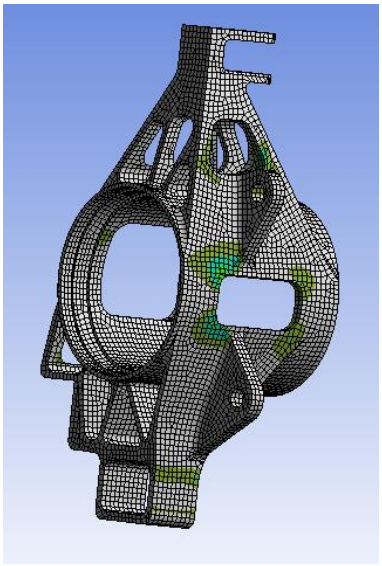

Figure 22: *Finite Element Analysis under maximum braking forces.*

The uprights will be made of Aluminum 7075-T6. A majority of the machining process will be done using a CNC mill and the rest will be done with an EDM wire. I expect the machining process will require 7 setups, one for each face of the stock, and the EDM for the holes. My first two steps will be to drill the holes that will be used for mounting the upper and lower A-arms in the top and bottom of the stock. I want to do this step first because I will be able to easily clamp the stock before too much material is removed. My next step is to remove the material for the holes on the side that doesn't have the brake mounts, again while there is enough material to easily clamp the stock. I will then mill the front and back surfaces where the bulk of the material will be removed. During this step, I will prepare the part for the EDM process and rough out the material for the holes to be cut. This last step will take a long time because the process will only cut around 15 to 20 thousandths of an inch per minute.

The Uprights are finished as of mid-February. During the first week of February it was discovered that the TM2 Haas in the machine shop was unable to cut precise circles and was out of operation. It took the Haas team 2 weeks to finish repairing the machine during which time Metro State University was contacted to help us continue to progress. We machined every day that Metro was at the shop and the machine was not being used by them and we were able to complete the project in the two-week span.

Each of the front uprights is 1.0lbs lighter than the previous iteration and each of the rear uprights is 1.5 lbs. lighter. Each of these parts should help to decrease corner assembly weight drastically and have a big impact on car handling performance.

Figure 23: *Completed Machined Uprights*

The major difficulties when making the uprights were associated with the complex setups. The original plan was to use gage blocks and toe clamps in order to hold the parts down for the secondary setups. But this method proved to be extremely complex and required a consider amount of time before the part would be clocked in the vice correctly. The solution was to make two sets of soft jaws, one for the front and one for the rear uprights. These not only made it extremely easy to get the upright clocked, and vertical but they also allowed the

secondary setup to be very stiff which meant that you could take deeper cuts with the endmill and not have to worry about the part moving too much while being machined.

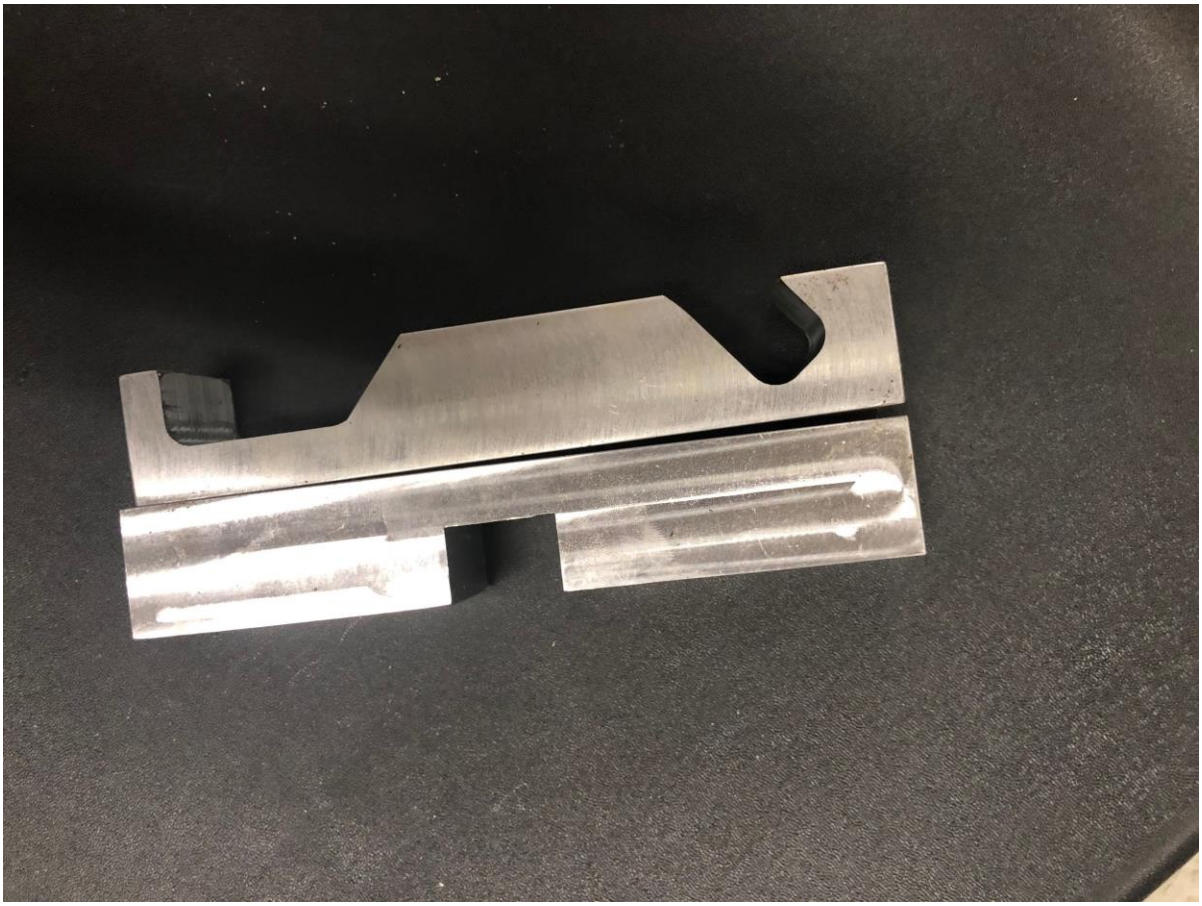

Figure 24: *Soft Jaws used during secondary setup Upright machining*

Anti-roll bar:

The Anti-roll bar or ARB is a suspension component of the car. The purpose of the ARB is to limit the amount of body roll of the chassis throughout sharp turns due to inertia. A vehicle not equipped with an ARB or an ARB that is too soft can experience excess body roll. Excess body roll can cause a series of issues that can lead to unwanted weight transfer, change of steering geometry, change of suspension geometry, lifting of tires, overloading the tire's available traction on the outside tires, complete loss of traction on the inside tires, and vehicle rollovers.

A car with a properly equipped ARB will allow the steering to remain more consistent to design parameters through sharp turns. During extreme body roll, the change of vertical displacement of the wheels can change the toe angle and camber of the front wheels resulting in unwanted steering geometry. The anti-roll bar can keep the control arms from moving excessively and keep steering geometry within design parameters.

A car with properly equipped anti-roll bars will keep the suspension geometry more consistent throughout turns. If a car experiences excess body roll, it can alter the geometry of the suspension leading to unwanted toe angles and changing the amount of camber. These changes in angle can lower the amount of traction available.

A car with properly designed anti-roll bars will help mitigate lifting the inside tires during hard cornering. When a car turns sharply, the inertia of the vehicle pushes the chassis in the direction that it was previously traveling. This lateral acceleration force acts on the vehicle's center of gravity and pushes the car towards the outside of the corner. When the car reaches its maximum load allowed by its suspension stiffness, it will start to lift the inside tires off the ground resulting in excess loading of the outside tires as well as complete loss of traction on the inside tires. The increased vertical load on the outside tires increases the amount of grip on the outside tires but also reduces the coefficient of friction thus reducing overall available traction.

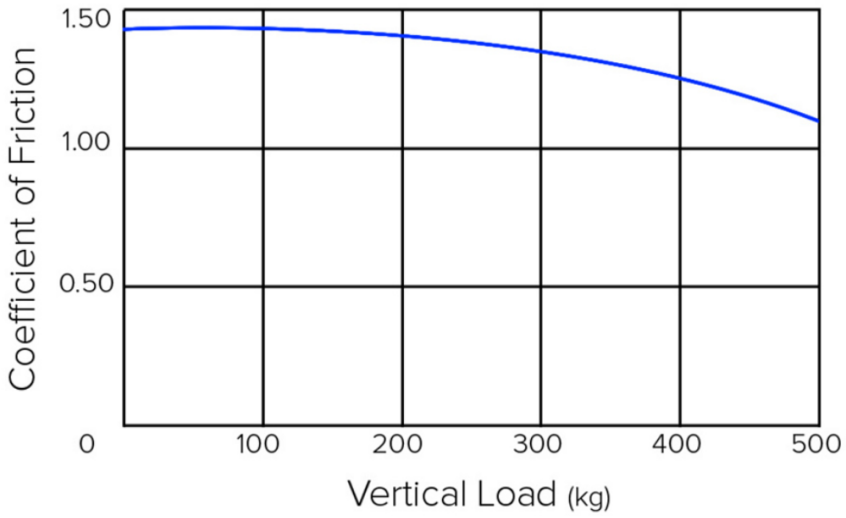

Figure 25: *Vertical Load vs Tire Coefficient of Friction*

Anti-roll bars can also increase driver confidence while driving by allowing the car to feel more planted and making steering input feel more direct.

The anti-roll bar in a car can be beneficial or hindering depending on the stiffness of the device. If the anti-roll bar is too soft, it can result in the same issues as not using one at all. If the front anti-roll bar is too stiff, it can cause understeer. If the rear anti roll bar is too stiff, it can lead to oversteer. Since the bar transfers forces from one side of the axle to the opposite side, a portion of the force caused by hitting a bump on one side will be transferred to the other side resulting in an unwanted disturbance in the suspension on the opposite side of the bump. If the anti-roll bar is too stiff, it can also cause an uncomfortable ride for the driver.

The spring stiffness due to torsion, KT, can be calculated with the force on the end of the anti-roll bar, P, the length of the anti-roll bar moment arm, R, and the angle of deflection, ϕ.

$$K_T = \frac{P}{R \cdot \phi}$$

The deflection at the end of the cantilever beam, K_B, can be found by using either the force on the end of the anti-roll bar and the deflection at the end of the anti-roll bar, xB, or by using Young's modulus, E, the moment of inertia of the bar, I, and the length from the bearing on the bar to the point where the end link attaches, L.

$$K_B = \frac{P}{x_B} = \frac{3EI}{L^3}$$

The overall stiffness of the anti-roll bar, KAB, can then be calculated.

$$K_{AB} = \frac{P}{x} = \frac{1}{\left(\frac{1}{K_T} + \frac{2}{K_B}\right)}$$

The anti-roll bar has been designed to be adjustable for stiffness as well as modular so parts can be replaced easily. The anti-roll bar consists of a torsion bar, two lever arms, two end links, two bearing bushings, two grub screws, two clevis pins, and two cotter pins to retain the end links.

Figure 26: *ARB Render 10/9/2019*

The moment arms are attached to the torsion bar by sliding over the ends of the torsion bar which are keyed to accept the moment arm without allowing them to rotate separately. A grub screw is then tightened to fix the two pieces together. This design allows for six levels of stiffness by allowing the end link to be positioned on different points of the moment arms. The distance from the central rotational axis of the torsion bar and the end link location is represented with R.

Position	R
Furthest hole	4.0 inches
2	3.6 inches
3	3.2 inches
4	2.8 inches
5	2.4 inches
Closest hole	2.0 inches

Table 1: *Anti Roll Bar adjustability*

By changing the value of R, the value for KT can be changed and the overall stiffness of the anti-roll bar in result, changes with it. The clevis pin that links the moment arm to the endlinks is retained with a cotter pin. This pin can be adjusted quickly and without tools allowing fine tuning on the track.

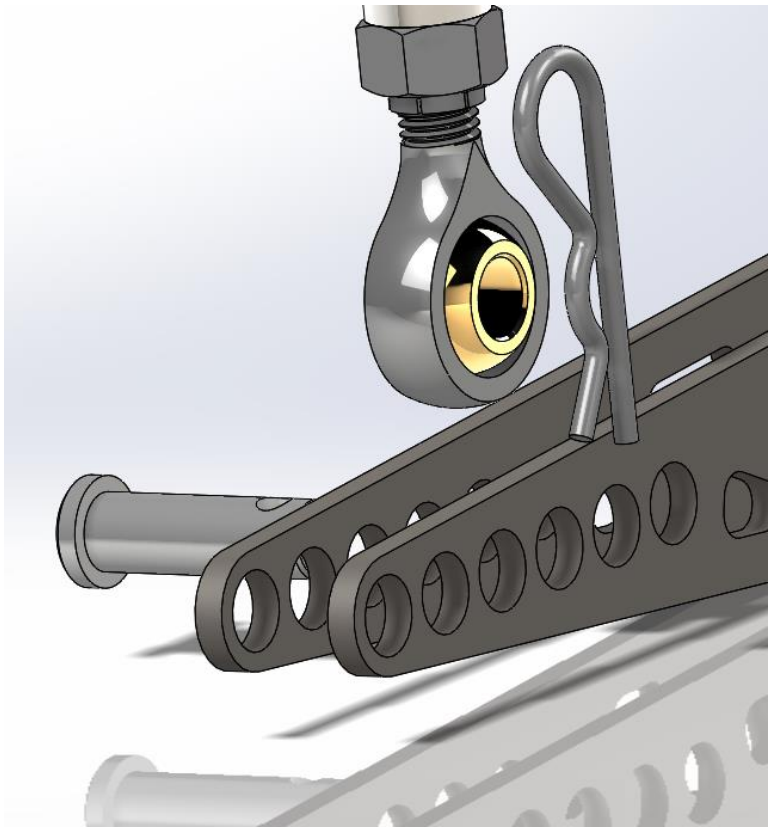

Figure 27: *Drop Links attachment exploded view*

ARB Free body diagrams:

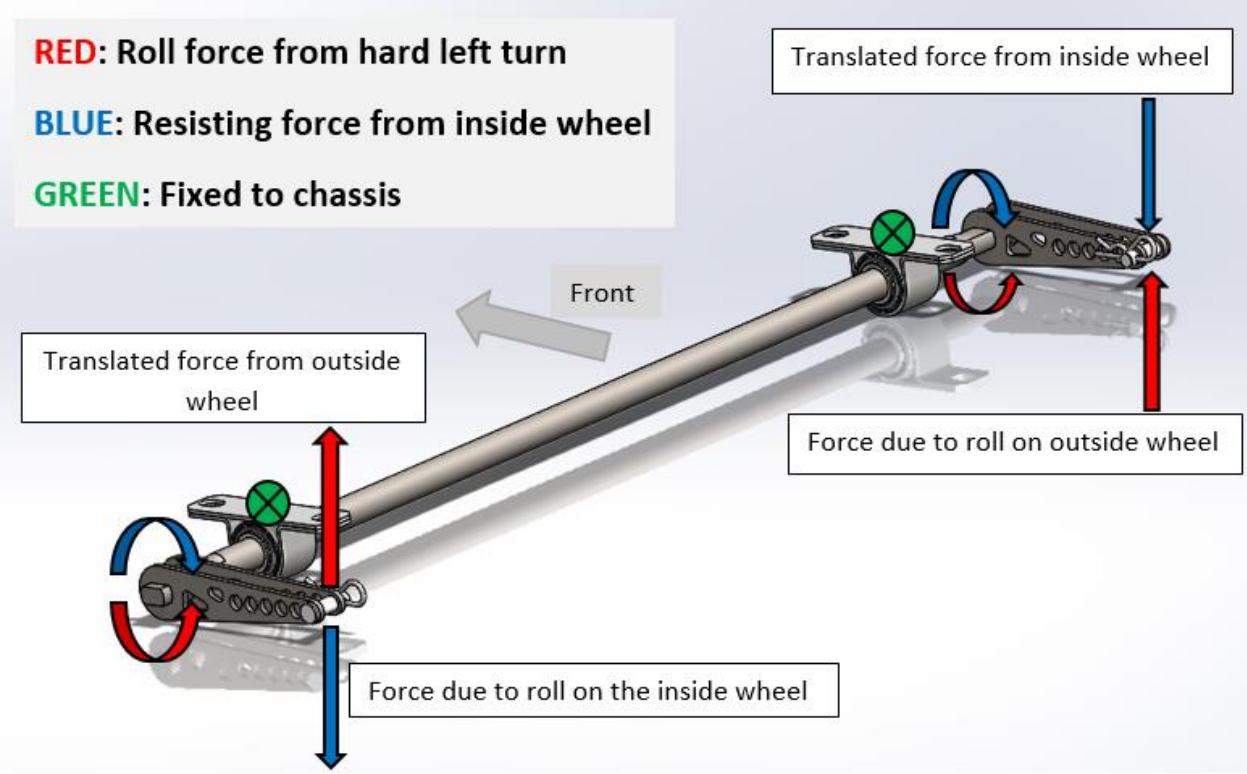

Figure 28: *Free body Diagram of Anti roll bar assembly*

The free body diagram in figure 28 shows how the upward force due to roll on the outside wheel is translated across the torsion bar and counteracted by the resulting drop of the inside wheel. The stiffer the torsion bar is, the more rotation is translated.

Finite element analysis simulations were tested on the model to determine the viability of the design. Each part was simulated through multiple tests with various conditions to optimize the design. The current model is the fifth revision of the original anti-roll bar. The torsion bar primarily takes an oscillating torsional force. The current torsion bar can withstand up to 267 ft lbs. The moment arms have been designed to sustain a load of 330 lbs at any of the adjustment hole locations.

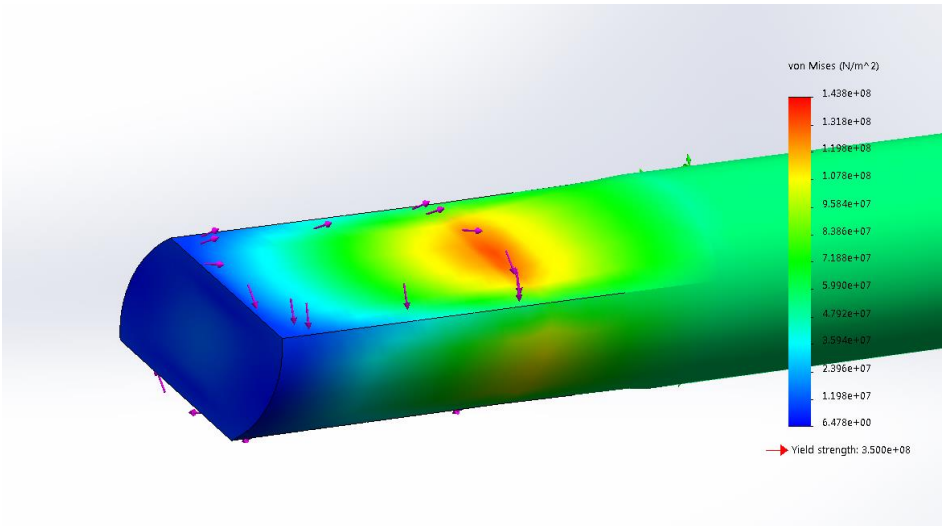

Figure 29: *Stress distribution on ARB torsion bar*

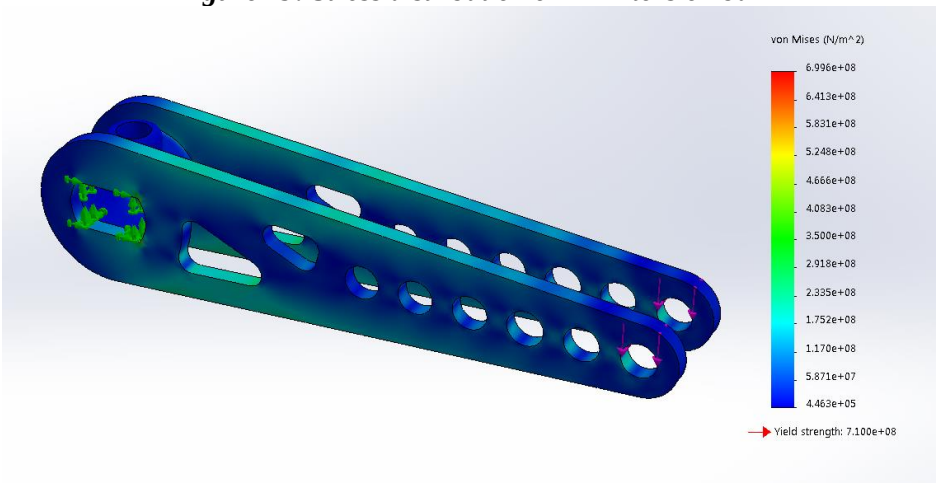

Figure 30: *Stress distribution of ARB drop link under 330lb force*

The ARB was completed in December. Welds were completed and the component is ready to be installed on the chassis when needed. The tabs for the ARB have been welded onto the chassis. The keyed components are held very tightly together as they hold a tolerance of .0003” between the bar and the moment arms. When the arms were welded together, there was enough deflection and expansion to seize the moment arms onto the rod. This will not matter because of the adjustability designed into the moment arms themself. The keyed components should not need to be removed unless there is a linear bearing failure, or the bearings need replaced. This is unlikely

and the moment arms can easily be pressed out with a hydraulic press. The adjustability component of the ARB remains as it was designed.

Looking back at the process and the development of the ARB, it would have been easier to just weld the moment arms onto the rod in the first place. If there needed to be any parts replaced the bar itself could be cut in half, bearings removed, and the ARB could be built from scratch in a short time. There was an issue with the placement of the ARB interfering with the exhaust and pingle mount. This was easily resolved by rotating the ARB 180 degrees and changing the length of the drop links. The adjustability remains as follows.

Position 1	39140 Nm/rad
Position 2	24492 Nm/rad
Position 3	16499 Nm/rad
Position 4	12000 Nm/rad
Position 5	9209 Nm/rad
Position 6	7082.11 Nm/rad

***Table 2**: Anti Roll Bar Spring Constant adjustability*

Figure 31: *Anti Roll bar completed assembly*

Control Arms

The analysis of the control arms was done using the forces found acting on the tire contact patch using optimumK. Using the kinematic sketch, it was possible to create vectors running between the mounting point on the upright and the mounting point on the chassis. An assumption was made that the knuckle, caliper assembly, brake disc and upright would all be treated as one rigid body. This assumption was made in order to prevent the need to account for the internal forces in the assembly. Six of the suspension members were analyzed: upper control arm (UCA), lower control arm (LCA), tie rod (TR) and push rod (PR).

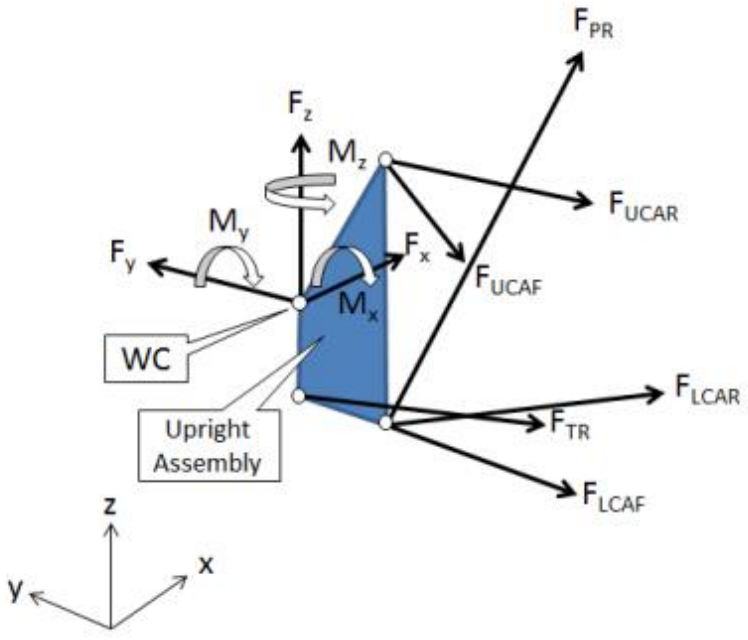

Figure 32: *Basic free body diagram of forces acting on the upright assembly, with the rigid body assumption made above*

From this free body diagram it was possible to balance forces on the contact patch with the forces and moments about the wheel center. These forces on the suspension members would be analyzed by constructing a matrix. Once vectors were made by finding the difference in

coordinates of the outboard (attached to the upright assembly) and the inboard (attached to the chassis), unit vectors were created to represent each member. From this these unit vectors *u*, the first three rows of the matrix were made using simple summation of forces in the x, y and z directions. The next step to creating the matrix was summing moments. In order to do this a wheel center in x,y and z coordinates was established. With these wheel centers a moment arm was created by subtracting the location of the wheel center from the outboard coordinate from each suspension member in the x, y and z locations. The moment sum equations were formed by taking the cross product between the moment arm and magnitude of forces. Now the 6x6 matrix could be formed.

$$[A] = \begin{bmatrix} u_{TRx} & u_{LCAFx} & u_{LCARx} & u_{UCAFx} & u_{UCARx} & u_{PRx} \\ u_{TRy} & u_{LCAFy} & u_{LCARy} & u_{UCAFy} & u_{UCARy} & u_{PRy} \\ u_{TRz} & u_{LCAFz} & u_{LCARz} & u_{UCAFz} & u_{UCARz} & u_{PRz} \\ (n_z r_y - n_y r_z)_{TR} & (n_z r_y - n_y r_z)_{LCAF} & (n_z r_y - n_y r_z)_{LCAR} & (n_z r_y - n_y r_z)_{UCAF} & (n_z r_y - n_y r_z)_{UCAR} & (n_z r_y - n_y r_z)_{PR} \\ (n_z r_x - n_x r_z)_{TR} & (n_z r_x - n_x r_z)_{LCAF} & (n_z r_x - n_x r_z)_{LCAR} & (n_z r_x - n_x r_z)_{UCAF} & (n_z r_x - n_x r_z)_{UCAR} & (n_z r_x - n_x r_z)_{PR} \\ (n_y r_x - n_x r_y)_{TR} & (n_y r_x - n_x r_y)_{LCAF} & (n_y r_x - n_x r_y)_{LCAR} & (n_y r_x - n_x r_y)_{UCAF} & (n_y r_x - n_x r_y)_{UCAR} & (n_y r_x - n_x r_y)_{PR} \end{bmatrix}$$

Figure 33: *This was the matrix formed from summation of forces and summation of moments, here u and n represent the unit vector formed for each member, and r represents the difference between the wheel centers and outboard points of each respective member*

Now it was simple to setup an x and B matrix to solve the forces acting on each member. Matrix B contained the forces acting on the tire contact patch and moments on the tire contact patch. Matrix x contained the forces acting on each suspension member

$$[B] = \begin{bmatrix} F_x \\ F_y \\ F_z \\ (F_z R_y - F_y R_z) \\ (F_x R_z - F_z R_x) \\ (F_y R_x - F_x R_y) \end{bmatrix}$$

***Figure 34**: This shows the matrix created from the forces acting on the tire contact patch and moments on the tire contact patch. R values were found by subtracting the wheel center location with the tire contact location, which made every Rx=Ry=0.*

$$\{x\} = \begin{bmatrix} F_{TR} \\ F_{LCAF} \\ F_{LCAR} \\ F_{UCAF} \\ F_{UCAR} \\ F_{PR} \end{bmatrix}$$

***Figure 35**: This shows the matrix we are attempting to solve for, in order to find the force on each suspension member.*

After putting these matrices in an Excel spreadsheet it was possible to solve for x by taking the inverse of matrix A and multiplying it by matrix B. Matrix B was changed for each critical load case: braking and cornering. By changing matrix B and solving for matrix x it is possible to know the largest loads each member will experience. Now knowing the forces each member will encounter possible to start considering design. One of the biggest factors in the

design of the control arms will be dependent on the size of pipe used. Currently an Excel spreadsheet is set up to change the outer and inner diameter of pipe and calculate the factor of safety using the critical buckling load equation and the max force equation.

The control arms are completed as of 3/18/2020 the only parts that are missing are the lower A-Arm tabs which connect the pushrods to the A-Arm assembly. All the Control arm inner bearing and outer bearing housings were completed over the winter break period and a rough total of 50 components have been manufactured in order to produce and properly weld the Control arms.

The major difficulties with machining the components have been due to the slow machining of 4130 Steel and the inability of the Haas CNC to cut perfect circles which caused the bearing fits on the bearing housings to slightly out of tolerance in one direction.

Figure 36*: Lower Control Arms Welded and Assembled*

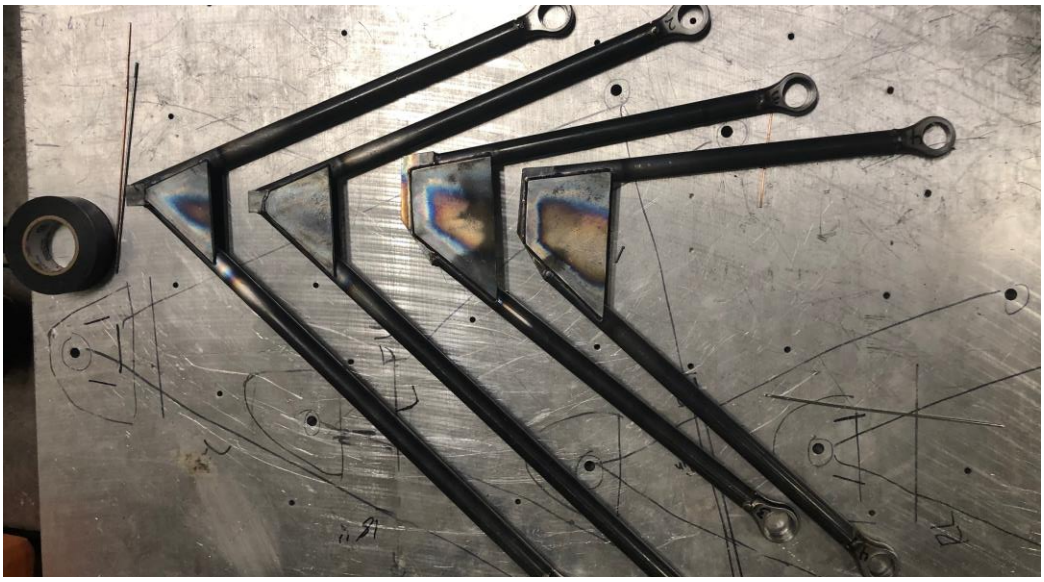

Figure 37: *Upper Control Arms welded and Assembled*

Figure 13: *The figure above shows the front A-Arm assembly (left) and the rear A-Arm assembly (right)*

Steering

The design for the steering assembly for this year's vehicle focuses heavily on driver feedback and interface. For the drivers to properly operate the vehicle during the event, they must be able to feel how the car reacts to the track and make adjustments as necessary. Upon inspection of last year's `car, it was found that there was a large amount of play in the steering, meaning that the driver could turn the steering wheel without the wheels moving. In addition, participants from last year's competition had expressed that the steering wheel was too low in the cockpit, resulting in an inability to comfortably steer the vehicle. Both issues will be addressed in this year's design. To mitigate the issue of play in the steering, the 2019-2020 vehicle will feature two mil. spec. single universal joints in place of the double universal joint from last year. Due to their high-precision construction, these "u-joints" should result in a tighter assembly. The

use of two u-joints also allows for the angle of the steering column to be changed so that the steering wheel does not impede the driver's ability to properly operate the vehicle.

By analyzing the track layout from years past, the administrative team was able to determine the ideal steering geometry for vehicle in order to be most successful during competition events. A 75-percent anti-Ackerman steering geometry was determined to be the best for this year's car. Ackerman steering is based on the concept that in order to properly maneuver a turn, the vehicle's front wheels need to turn at independent rates to optimize tire contact with the track. A steering system utilizing 100-percent Ackerman steering is constructed such that the inner wheel turns at a higher rate than the outer wheel. This difference in turn rates results in a geometry that, when lines are drawn normal to the tires, they intersect at the center of the turn, in line with the rear axle. Anti-Ackerman refers to a geometry where the outer wheel turns quicker than the inner wheel. Figure 38 shows the difference between these steering geometries. Anti-Ackerman geometry increases the slip angle on the outer tire, resulting in more grip through turns during low to mid-speed turns. It was calculated that 75-percent of all turns in autocross and endurance are mid to low speed, which makes this geometry ideal for the competition.

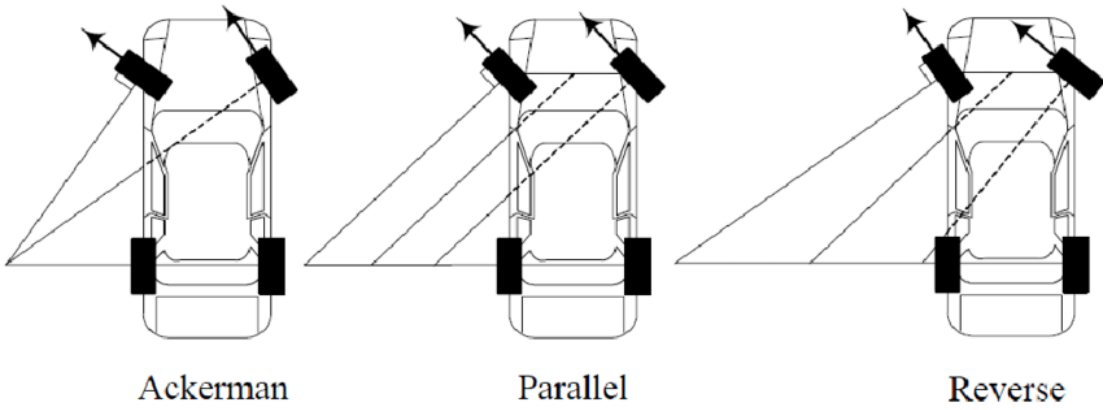

Figure 38: *Ackerman, Parallel and Reverse (Anti-Ackerman) Steering Geometries (Wardana)*

Proper steering geometry is accomplished by connecting the rack assembly to the wheel uprights in a location that minimizes bump steer, maximizes grip on the track, and optimizes cornering. Using OptimumK simulation software, this ideal pickup point was determined. This point was determined to be 1.69 inches forward of and 2.261 inches below the front axle center (see Figure 39). Figure 40 shows the OptimumK graph showing the relationship between steering angle and heave. It shows that for a heave distance of 2.5 inches, the steering angle is only affected by approximately 0.3 degrees. The relationship between these motions are known as bump steer. From the pickup point, the tie rods and rack will extend linearly to the center of the vehicle, which then connects to the steering column. By maintaining this linear geometry, bump steer is minimized.

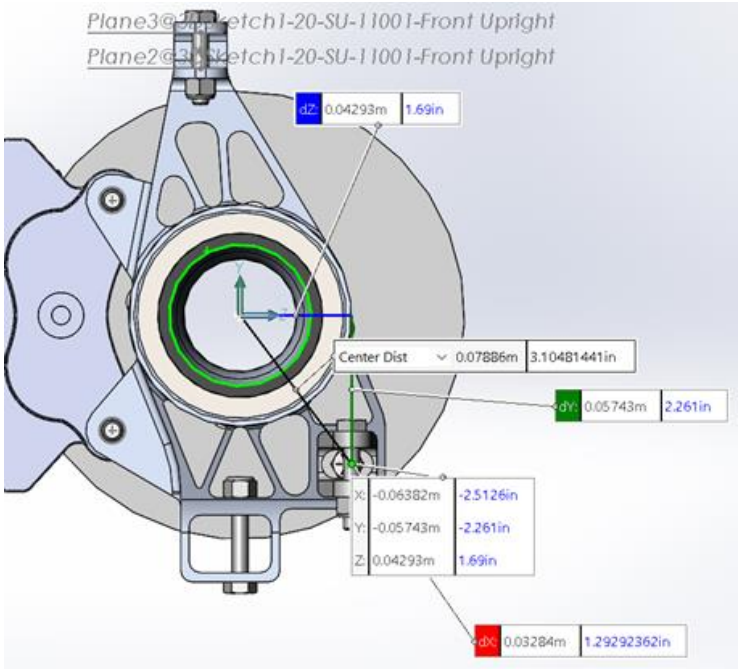

Figure 39: *Detail View of Tie Rod Pickup Location*

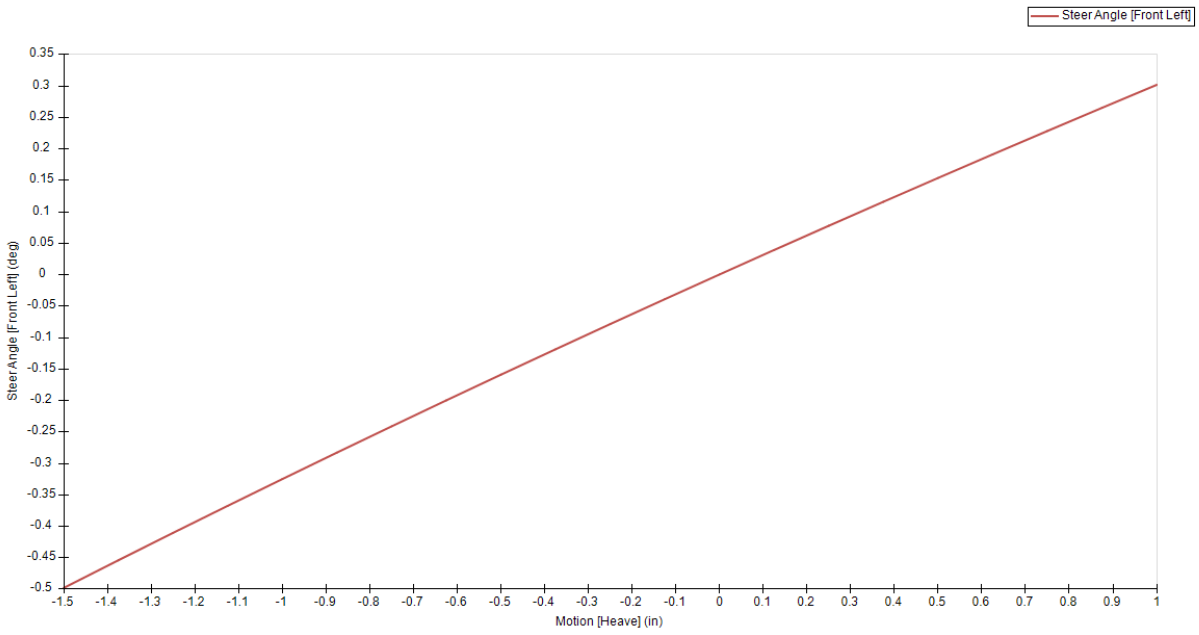

Figure 40: *Analysis of Steering Angle vs Heave*

Another major change in the steering assembly design is the steering column material and geometry. To reduce the overall weight of the assembly, a pultruded carbon fiber rod is replacing the steel steering column. By changing materials, the steering column weight is reduced from approximately 2 lbs to approximately 0.2 lbs. Both ends of the rod will be milled flat on one side to index the rod into the u-joints, which assists with torque transmission. Finite element analysis was performed on the rod with an applied torque of 25 N-m and passed with a factor of safety above 2 (Figure 38). This torque is a generous estimation of the maximum force that the steering column will experience. Maximum steering torque will be experienced when the car is stationary and will only decrease as the car is moving. The carbon fiber will be attached to the u-joints by potting it using resin as well as a ¼-20 bolt through the assembly. Formula SAE rules require that adhesive attachments must be reinforced with a mechanical support.

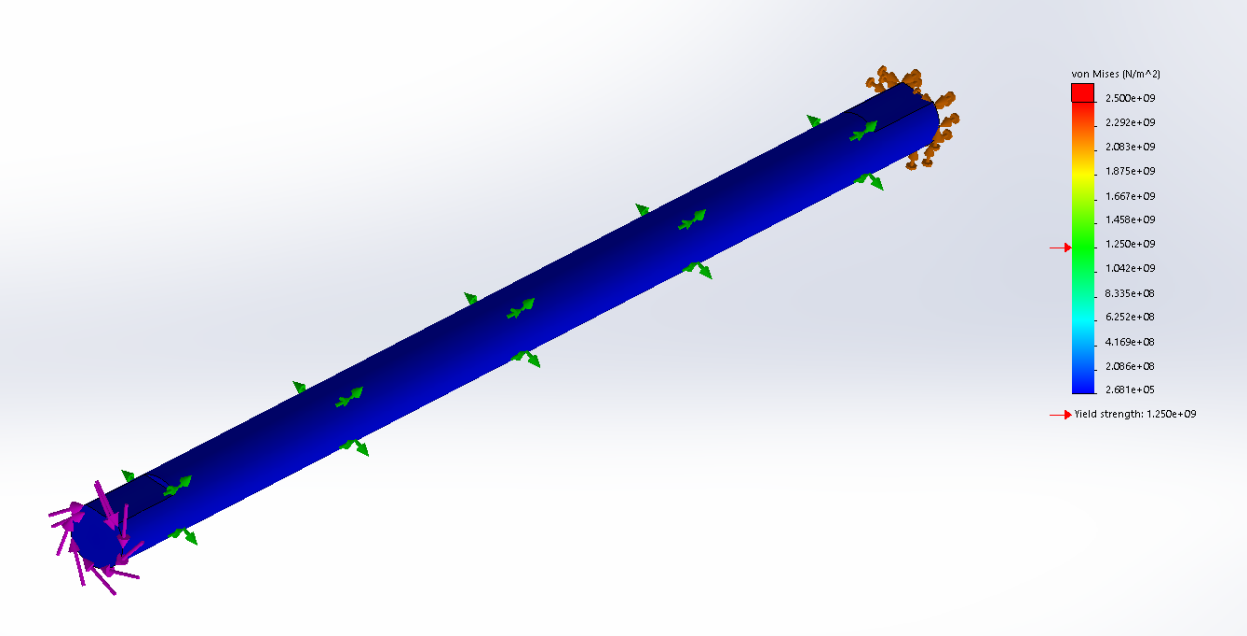

Figure 41: *Finite Element Analysis of Carbon Fiber Steering Column*

Other components in the assembly include the steering wheel quick connection hub, the frame mounts, and the tie rods. Over the next few weeks, all components of the steering assembly will be tested using FEA, and manufacturing will begin shortly after.

Figure 42: *Rendering of Steering Assembly*

By the end of last semester, the steering column, quick release hub and rack and pinion were the only components that had been manufactured. While the chassis was being assembled, the steering attachment tabs took priority. In order to assure proper function of the assembly, a steering column angle of 25.5° above the horizontal is required, so a four-piece sheet metal bracket was designed and fabricated to attach the rack and pinion to the chassis at this angle. The bracket was made of ⅛” 4130 chromoly steel and is attached to a horizontal member of the chassis below the legs of the driver. The bracket attaches to the rack and pinion using ⅜-inch SAE grade bolts. Production of this part only took a day.

One of the biggest challenges that the team faced in the steering assembly was specifying components that mate to pre-existing components from last year's car. The areas of the steering assembly most impacted by this challenge are at the rack and pinion and the steering wheel attachment sites. In order to attach the lower u-joint to the rack and pinion, the Stiletto rack has a spline that was specified by the manufacturer as a ⅝-36 spline. After many weeks of research, it was found that this spline geometry is not outlined in any ANSI or ISO standards. The original plan for this attachment point was to utilize the sinker EDM to bore the spline into the u-joint, but instead, a coupler component with the spline geometry was purchased, and a circular bore was drilled in the u-joint that was under-sized by 0.003" to accommodate a proper press fit between the coupler and the u-joint. An additional problem area on the steering system was at the attachment site of the steering wheel to the assembly. The steering wheel features a quick release mechanism that allows for easy removal of the steering wheel for driver entry/exit. The quick release mechanism features a 16 spline geometry with a single spline wider than the others to allow for proper indexing of the steering wheel. The steering wheel attachment hub profile was roughed out using the Haas TL-2 lathe, and the only remaining feature on this component is the spline geometry to mate to the steering wheel. This spline will be machined onto the hub using the sinker EDM with a female electrode. In order to ensure proper fitment, test splines were cut on the wire EDM out of 1-inch aluminum stock and inserted into the steering quick release. Two iterations of this spline were created, one with a deeper root diameter than the other. The deeper root diameter geometry was chosen, as the shallower root diameter spline did not fit into the mating part. Although the geometry does not exactly match that of the quick release component, an FEA simulation was performed to ensure that the splines could withstand an applied torque of 100N-m. A factor of safety of 2 was found at this component, leading to

confirmation of this geometry for the spline. Production of sinker EDM electrodes will be underway within the next week.

Following production of the sinker EDM electrodes, the only remaining components to be manufactured for the steering assembly are the upper chassis mount and bearing housing. The decision was made to save these components for last, since the angle and position of the steering wheel is based highly on driver input. Once all other components are manufactured and attached to the vehicle, simple brackets and bearing housings can be manufactured quickly.

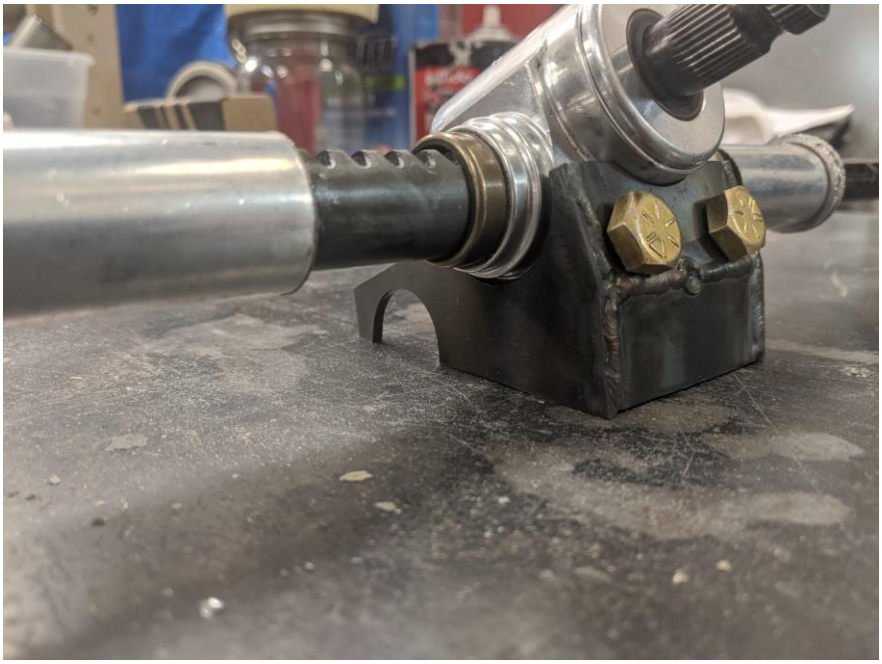

Figure 43: *Sheet metal bracket to attach rack and pinion to the chassis*

Figure 44: *Final attachment of rack and pinion to the chassis*

Figure 45: *Comparison of this year's steering wheel attachment hub (left) to last year's component (right).*

Figure 46: *Steering u-joints and carbon fiber steering column.*

Braking

The rules state that the car must be capable of simultaneously locking all four tires during a brake test. The car is required to have two master cylinders for two separate brake lines so that a failure in one line doesn't compromise the braking system. The car is going to weigh 670 lbs and will have a downforce of 130 lbs while moving at its average speed of 44 mph. Under 1.5 g's of braking force, the car will have 72% of its weight on the front tires and 28% on the rear.

In order to lock the tires, a torque equal to the torque applied on the tires by the road will have to be applied to the rotors. The pedal force applied by the driver is transferred by a lever which multiplies the force outputted to the pushrod which pushes the master cylinders in. A pedal

force of 65 lbs was chosen to lock the wheels and used for calculations. The master cylinders displace an incompressible brake fluid which travels along the brake lines and into the brake calipers. The fluid is displaced into the one or two pistons on each side of the calipers. This pushes the brake pads into the rotors and creates a friction force which generates the braking torque.

One of the design constraints was to be able to fit the rotors and calipers inside the new wheel which meant a rotor outer diameter had to be under 7.5". A diameter of 7" was chosen for the design. Grey cast iron was used for the material for its thermal properties, friction performance, and machinability. Another constraint was keeping the line pressures down below a maximum pressure of 1500 psi that Wilwood's master cylinders can handle. A minimum safety factor of 1.5 was chosen for the pressure. To keep the pressure low while still reducing the rotor diameter from last year, two different calipers will be used. The GP 320 which has 4 pistons and will be used for the front and the PS-1 which has 2 pistons will be used for the rear. Since the front rotors require a higher braking force, larger calipers can be used to increase the force applied to the front calipers so that a lower pressure can be used. With the design, a pressure of 644.7 psi will be in the front brake lines and a pressure of 712.0 psi will be in the rear brake lines. Hard lines will be used over soft lines for as much of the brake lines as possible in order to reduce brake line expansion which can lead to a loss of braking efficiency. The front brake pads have a coefficient of friction ranging from 0.54 to 0.64, and the rear pads have a friction coefficient of 0.48.

The ratios between the piston areas of the calipers and the master cylinders for the front and rear need to be about equal since the master cylinders must travel the same distance. The distance that the pistons travel is based off the amount of fluid that is displaced in order to bring the pads in contact with the rotors. The fluid displaced into each caliper is equal to the clearance between the pads and the rotor times the total area of the caliper pistons. For each pair of calipers,

this fluid is displaced by one master cylinder. From geometry, the travel of the pedal can be found with the following equation:

$$pedal\ travel = \frac{2\,\frac{a}{b}\,l_{\ clearance}\,A_{\ caliper}}{A_{\ MC}}$$

With a mechanical advantage of 6.5:1, a pedal travel of about 2.5" was found.

The brake rotors will be designed to facilitate material removal from the surface by adding slots and scalloping the edges which can be seen in Figure 47. This will also help with weight reduction and increasing the surface area for convection and radiation. The brakes need to be able to survive a combination of shear stresses, thermal stresses, and centrifugal stresses. Also, since the stresses will be applied in a cyclic manner, fatigue must also be accounted for. Thermal stresses can be calculated using the following equations:

$$\Delta T = \frac{q}{c_p m}$$

$$\sigma_{\ thermal} = -\frac{E}{1-v}\,\alpha_T \Delta T$$

The centrifugal stress can be found using FEA. The heat flux into the rotor is equal to the heat generated by friction divided by the surface area of the rotor that is in contact with the pads and divided by the braking time. The heat transfer coefficient h will be found using CFD by simulating the air swirling around the disk at the car's average angular velocity. This will be added to a radiative heat transfer coefficient which varies with temperature with an emissivity value of 0.55 being used in order to calculate an overall heat transfer coefficient. A thermal model will be created to find the steady state value of the temperatures for cyclic braking over a large period of time. Heat transfer equations can be used to find the steady state temperature for repeated braking and the cooling response over time.

Figure 47: *Current design for braking rotor*

Another method involves using FEA to model a step input response for heat flux into the rotor with heat being removed by convection and radiation. This required doing research in order to find the average braking frequencies and velocities so the amplitude and frequency of the step input could be made. One FEA result under repeated braking can be seen on Figure 48. The temperature of the rotor should stay under 750C and ideally be under 650 C which is where brake fade starts to occur for the front brake pads. The design of the rotors will be changed in order to facilitate heat transfer and minimize weight while maintaining a safety factor of 2 for stresses.

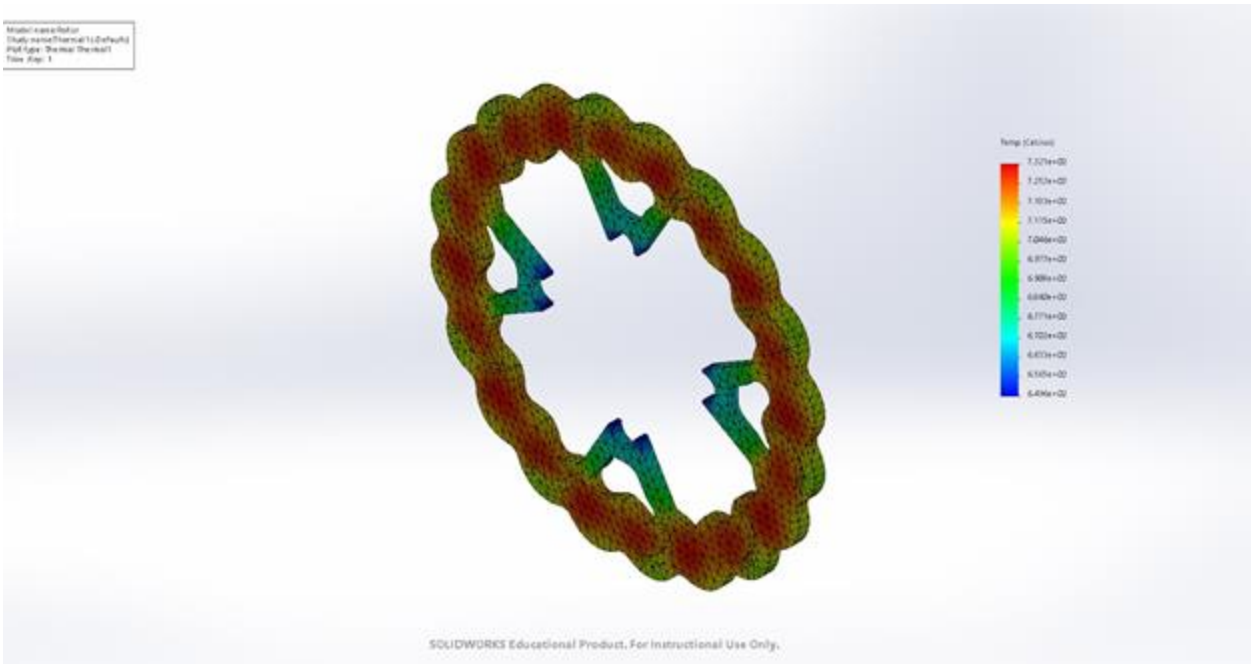

Figure 48: *Thermal FEA for repeated braking*

The master cylinders, hard lines and brake pads have come in. The master cylinders have been installed on the pedal box and brake lines are being planned out.

The rear brake rotors were redesigned and re-machined to be put on and removed from either side of the hubs. This adjustment also led to some weight reduction near the inner profile of the rotor without compromising material in the braking zone. FEA was reran on the new rotors to ensure a similar safety factor and thermal performance was achieved, though the safety factor and thermal performance was already high given the much lower braking forces on the rear rotors.

The rotors were machined from 10” ASTM A48 Class 40 grey cast iron rotor blanks using a CNC mill with ⅜ flat, 3/16 flat, and ⅛ ball end mills. Each operation was done with one finishing pass and two step downs were required when using the 3/16 flat end mill. The part was held down by three clamps on the outside and all of the inner pockets and slots were milled. Then the part was flipped and held down from the center and one of the pockets so the outer

profile and the slots on the other side could be milled. The machining time per rotor was about three hours with about half an hour of setup. A machined rotor can be seen from figure 49. Some of the cuts made through the rotor didn't reach the bottom of the stock, so edges were cleaned up with a Dremel tool.

Figure 49: *Machined rotor*

Chassis

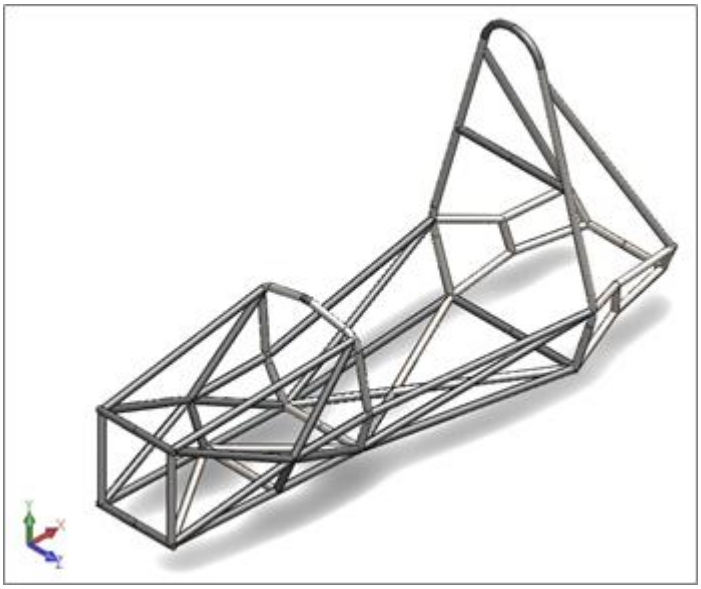

Figure 50: *Current Chassis Model.*

The chassis can be viewed as the main component that will bring the entirety of our FSAE project together, acting as the skeletal system that every other manufactured component in the project will be attached to. In addition to acting as a centralized hub for component connections, the most utmost important duty of the chassis is to protect its precious cargo; the driver. Figure 51 from version 1.0 of the FSAE 2020 rules gives an idea how the driver will be protected within the chassis, encompassed by structural members.

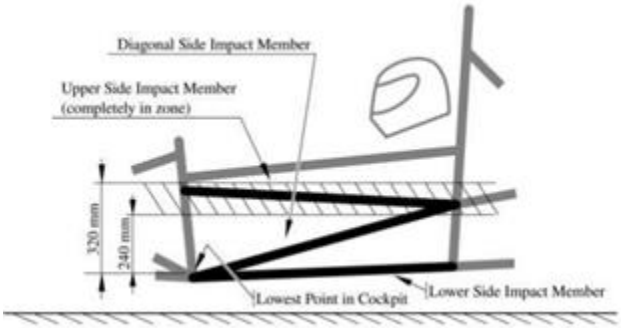

Figure 51: *Driver's compartment Rules*

This year's chassis is composed of over 50 structural members, weighing in at a mere 64 lbs., for this year's collegiate competition. A substantial reduction in weight over last year's chassis design at a 33% weight reduction! The chassis is comprised of three main transverse tubing planes that are then adjoined to each other with several longitudinal tubing members, including the critical side-impact members. The three main transverse tubing planes are: the front bulkhead, the front roll hoop, and the rear roll hoop.

Per the 2020 FSAE rule set, four main tubing sizes have been deemed acceptable for the manufacture of the chassis for the 2020 competition. Table 4 lists these tubing sizes as their outside diameters and respective wall thicknesses.

Tube Size:	Round Tube Size
A	1.0" X 0.095"
B	1.0" X 0.065"
C	1.0" X 0.047"
D	1.375" X 0.047"

Table 3: *FSAE 2020 required tubing outside diameters and wall thicknesses*.

For our design, we have decided to forgo any design considerations with that would include the 1.375 inch outside diameter tubing size, and instead focus on the three 1.0 inch outside diameter tubing sizes for shear simplicity. Several constraints are outlined within the 2020 rule set that dictate specific tubing sizes that must be utilized in certain positions on the chassis. An example of this would be the requirement for the rear roll hoop to be constructed out of the 1.0 X 0.097" tubing size, the most robust tubing wall thickness recommended by FSAE. In every applicable scenario, our design went with the default tubing wall thickness size as dictated by the 2020 FSAE rule set. Additional design considerations will be made once FEA analysis is complete to determine if tubing members without a sizing requirement can be exchanged with a lighter member. Figure

52 depicts the current configuration of tubing size selections as per FSAE rules. Green representing the largest wall thickness, and yellow being the thinnest.

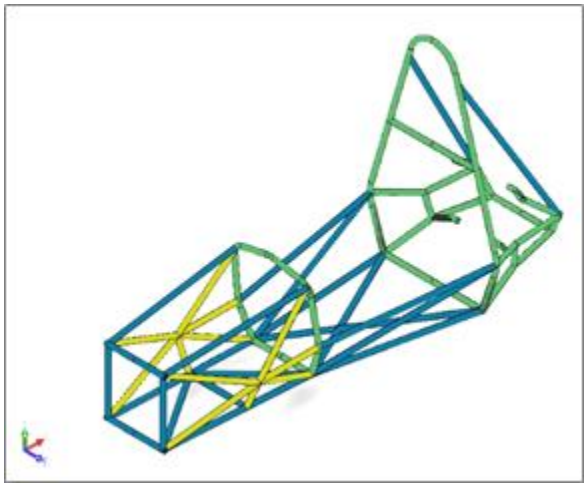

***Figure 52**: Chassis model with colorized tubing members representative of size.*

In addition to the dimensional constraints that have been placed on the selection of tubing sizes, several material property considerations must also be made per the FSAE 2020 rules. FSAE sets requirements that state any steel used in the manufacture of the chassis must meet or exceed minimum values for: elastic moduli, along with the respective ultimate and yield strengths. To adhere to these guidelines, the entirety of the chassis will be manufactured out of readily available 4130N Cr-Mo aircraft grade steel tubing.

Preliminary analysis of the chassis has begun using the ANSYS 2019R2 software package. This software allows for the uploading of the 3D chassis model so that finite element analysis may be run. The main objective with the ANSYS software is to analyze the frame's compliance through a torsion test. This torsion test aims to replicate the forces exerted from the tires' contact patches to the frame. The forces are diagrammed in figure 53 at points B and C, with the rear of the car simply supported at the rear bulkhead corresponding to position A.

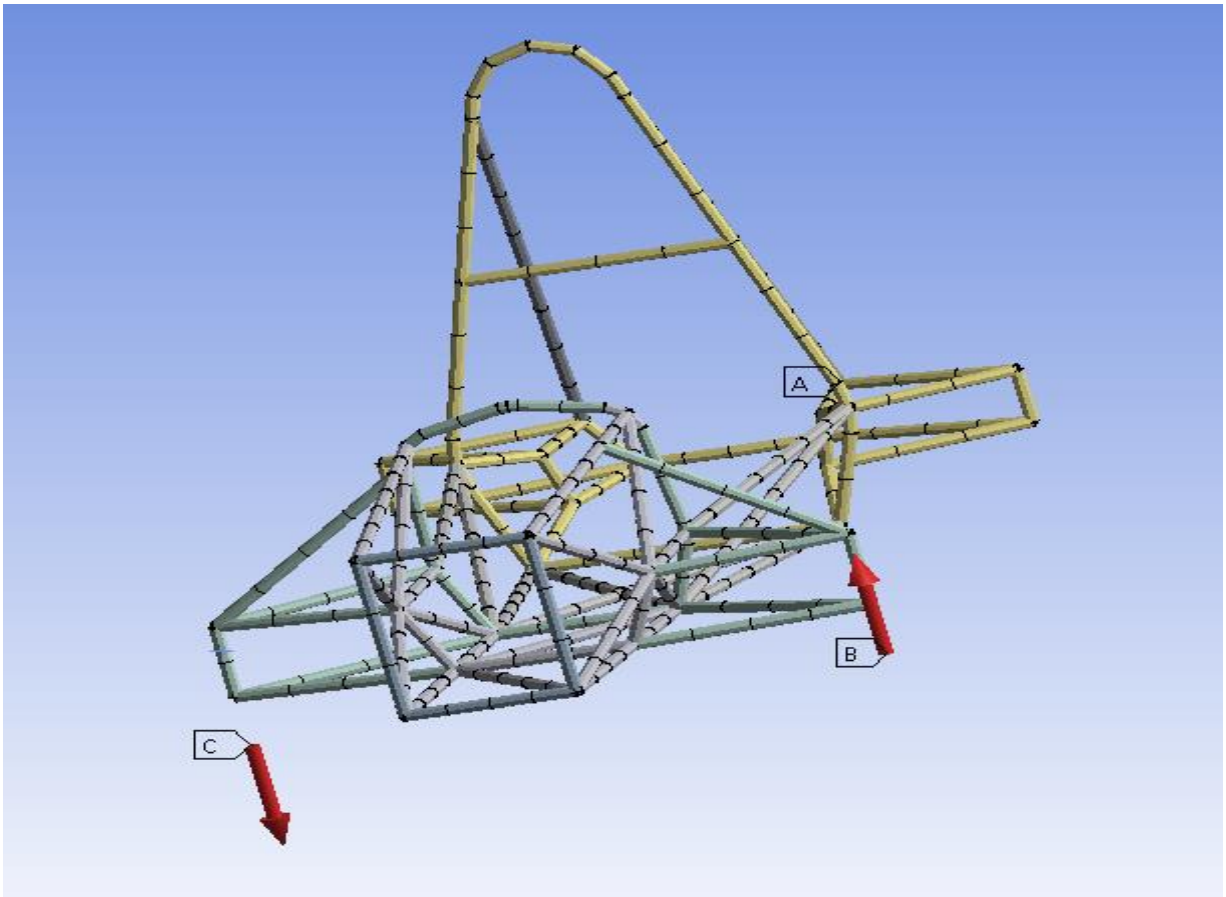

***Figure 53**: Chassis model with forces displayed in test for torsional rigidity.*

The units of measurement for this torsional rigidity test are in ft-lb/degree. The 2018-2019 Lynx Motorsports vehicle claims a (simulated) 1340 ft-lb/degree. A tutorial published by ANSYS for developing FEA simulations for FSAE chassis was followed. Using ANSYS to prescribe a 1 degree deformation along the line between the two front tire contact patches, the torsional stiffness comes out to 921 ft-lb/degree. This 31% reduction in stiffness could be attributed to the reduction in frame members to lighten the chassis. It could also be attributed to a different design of the FEA test, or even a use of ANSYS instead of Solidworks. Stiffness and weight are tradeoffs. More iterations of FEA are needed to optimize the frame further for stiffness vs weight.

Future tests will involve the suspension design team to ensure that the rigidity of the frame remains negligible relative to the suspension kinematics. Additionally, last year's frame will be placed into

the FEA software package and tested in the same manner as the current frame in order to eliminate error.

Figure 54: *Current Chassis Model.*

The general chassis design has remained nearly untouched since preliminary design review occurred. The need for changes to the design arose when inputting chassis specifications into FSAE's Structural Equivalency Spreadsheet (SES), as well as minor manufacturing limitations from the material supplier, VR3. Once modifications were made, design specifications were rechecked against SES requirements, along with additional FEA analyses to confirm design requirements. Upon entering the chassis specifications into the SES, it was evident that several problems existed within the initial design. The rear subframe had not been properly triangulated. The upper member of the side impact structure was positioned too far below the top of the front roll hoop, additionally two radii within the front roll hoop did not meet the required minimums. Triangulation of the rear subframe was accomplished by the addition of several diagonal members, albeit at a weight penalty. These additional members were oriented such that they would not generate any interference issues with rear axle displacements, a preliminary concern within the design changes. Repositioning of the side impact member was further complicated by the locations for several of the suspension mounting tabs for multiple front suspension components. To avoid further modifying the locations of the mounting tabs, and thus necessitating a full front suspension redesign, an additional structural member was positioned such that, the point where the now raised side impact member meets the front roll hoop would be properly triangulated per SES requirements. The raising of this side impact member, generated an increase in overall torsional rigidity of the chassis, as confirmed with subsequent FEA analysis. As a result of raising the side impact member, one of the two diagonal members that were initially bracing the side impact structure was able to be discarded from the design entirely. Radii within the front roll hoop were enlarged without affecting other structural members.

Additional revisions to the chassis design were made as a result of manufacturing limitations placed by the material supplier, VR3. VR3's tooling specifications define certain centerline radius dies to be utilized within the chassis' bend features. Initially defined radii within the front and rear roll hoops did not match those as specified by VR3 and needed to be subsequently modified within the design to meet the supplier's tooling specifications.

Despite the addition of several tubing members, the chassis weighs in at a mere 68lbs; a minor setback from the initial design of 64lbs, though still an improvement over the 2019 Lynx Motorsports chassis weight of 73 lbs.

Several considerations were made into the manufacturability of the chassis design throughout the entirety of the process, with the ever-present mindset of design it how it would be built on the shop floor. Careful attention was paid to the trims/extends that were applied within Solidworks to produce a final product with the appropriate fitment. Tubing wall thickness requirements were updated per the SES and FEA specifications.

As it stands, the current iteration of the chassis has been "approved for manufacture", and the required documentation provided to the material supplier, VR3. VR3 will section and cope the 73 structural members required for the chassis manufacture and deliver a product ready to weld upon receipt. Anticipated arrival of material from VR3 is by the end of December 2019.

In the meantime, design has begun on a jig system that will be utilized in the manufacturing and welding of the chassis. The jig system will act as a series of templates that help to align the multitude of tubing members prior to welding. Careful attention was paid while modeling the chassis jig to ensure the sequence of events within the manufacturing of the chassis will remain logical and well organized throughout the entirety of the process.

Powertrain

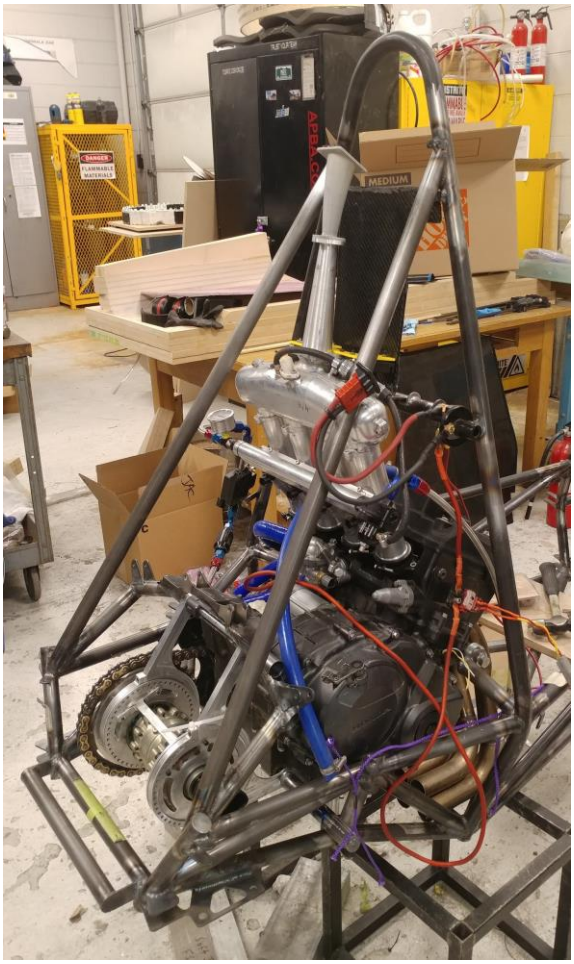

Figure 55*: Engine in the chassis*

The engine this year will remain the same as previous years with it being the 2007-2012 Honda CBR600RR. We are using the same engine as the previous three years because we are familiar with this engine and have three years of experience tuning it. The intake and exhaust that were developed and manufactured last year will be used again this year as we don't have the manpower or time to re-develop and re-manufacture these parts. We will be using the Motec C130 ECU (Engine Control Unit) this year as well. The Pingle shifting system will be used again this year too and the gears will be changed through shifter paddles on the steering wheel. The current powertrain assembly is shown above in *Figure 55*.

We are currently looking for a new or used 2007-2012 engine as the current 2007 engine in the car has low compression and piston cylinder wall scoring. A healthy CBR600RR engine should produce compression of 180 psi across all four cylinders but the current engine produces compression of 155 psi when warm. The piston cylinder wall scoring has been said to be normal for these engines after extended use but ideally we would like an engine with no scoring which causes engine blow by. Engine blow by is when the air and fuel mixture escapes past the piston rings and goes into the crankcase in the engine, this makes the engine less efficient. The blow by effect can also bring oil from the crankcase into the piston cylinders which can then lower the effective octane rating of the air and fuel mixture. If the octane rating drops low enough the engine can then start experiencing knock where the fuel mixture ignites before the spark plug can ignite the mixture and this causes high cylinder pressures which can then destroy the engine.

Since the current engine that is in the car has been used for three seasons we think it would be a good idea to find a different engine with higher compression and no piston scoring so we wouldn't have to worry about any reliability issues related to the engine block. The engine internals will remain stock to help improve reliability. We are looking at spending a maximum of $1200 for a new engine.

The same oil pan that has been on the car will be used again unless we have some additional time to machine a new oil pan later in the year since the current oil pan has some scratches on it from the past three years of use. None of the scratches seem deep enough to cause any problems so manufacturing a new oil pan is not a high priority.

Over winter break the engine cylinder head was rebuilt and the engine has been placed into the chassis and on March 8th was started for 20 seconds. In order to determine if the head rebuild was done correctly it was important to get the engine in the car and started. While running the engine the cylinder head seemed to be working properly but the engine needs to run longer to ensure the rebuilt head is ready to race with. The engine was run for such a short period of time because the exhaust and fuel tank were

not completed yet at the time of the start up and the radiator was not on the car. ***Figure 55*** shows the engine in the chassis and the engine wired up to run.

Exhaust

The Fall 2019 exhaust design featured a 4-2 collector and a 2-1 collector (Figure 56). This design is normally called a Tri-Y design and generally preferred when better mid-range torque is needed. Due to machining limitations, the 2-1 collector was difficult to manufacture because one portion of the collector had to be offset at an angle inorder to stay within chassis limitations and not interfere with other components of the car. After several failed attempts at producing a suitable 2-1 collector, the Fall 2019 design was scrapped in favor for a 4-1 collector. The benefits of a 4-1 collector is it's compact design and better peak torque. This design was originally not preferred because the car is currently traction limited, and peak torque is not an issue; however, being able to route the exhaust within the limited available space was more important. The current plan is to manufacture the 4-1 collector, but if the same manufacturing issues arise, standard 4-1 collectors are available for purchase, albeit at a premium price.

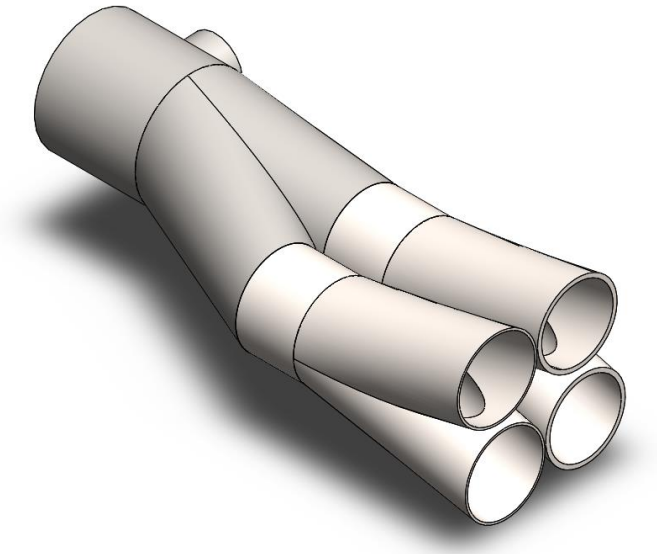

Figure 56: *Fall 2019 Tri-Y Design*

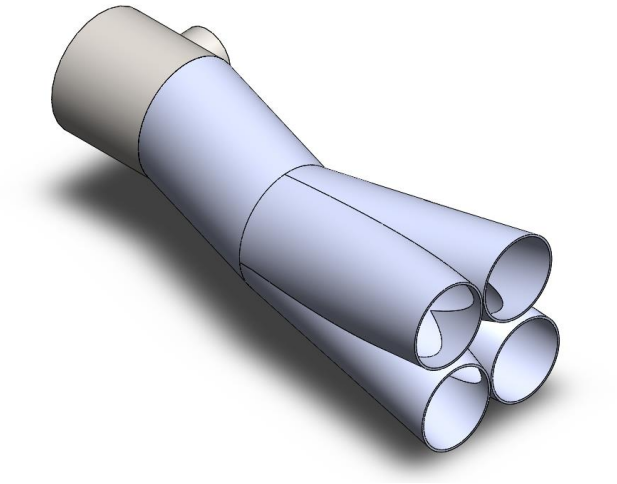

Figure 57: *Spring 2020 4-1 Collector*

Axles

Due to the smaller chassis and lighter car, the rear axles needed to be trimmed from 16 inches down to 14 inches. Since the axles were made of hardened steel, they were cut using the metal cutting wheel, and then cut to proper size using the lathe. Additionally, the hardened steel made it difficult to work with on the lathe, and even with the use of specially ordered carbide bits, the process to trim, face, and groove the axles took several hours of machining time and several bits were chewed up in the process.

Figure 58: *Rear Axles*

Fuel System

The car this year will continue using E85 fuel as the primary fuel. The reason we are continuing to use E85 is because one of our biggest monetary sponsors is Colorado Corn and we have the most experience tuning with E85. We plan to incorporate a flex fuel sensor which will be able to determine the ethanol content of fuel we are putting in the car and will be able to adjust the tune accordingly. E85 tends to vary in ethanol content depending on geography and season, usually from 51% to 83% ethanol (Fueleconomy.gov, 2019). By incorporating a flex fuel sensor this should help the engine maintain optimum performance with E85 which has varying ethanol content.

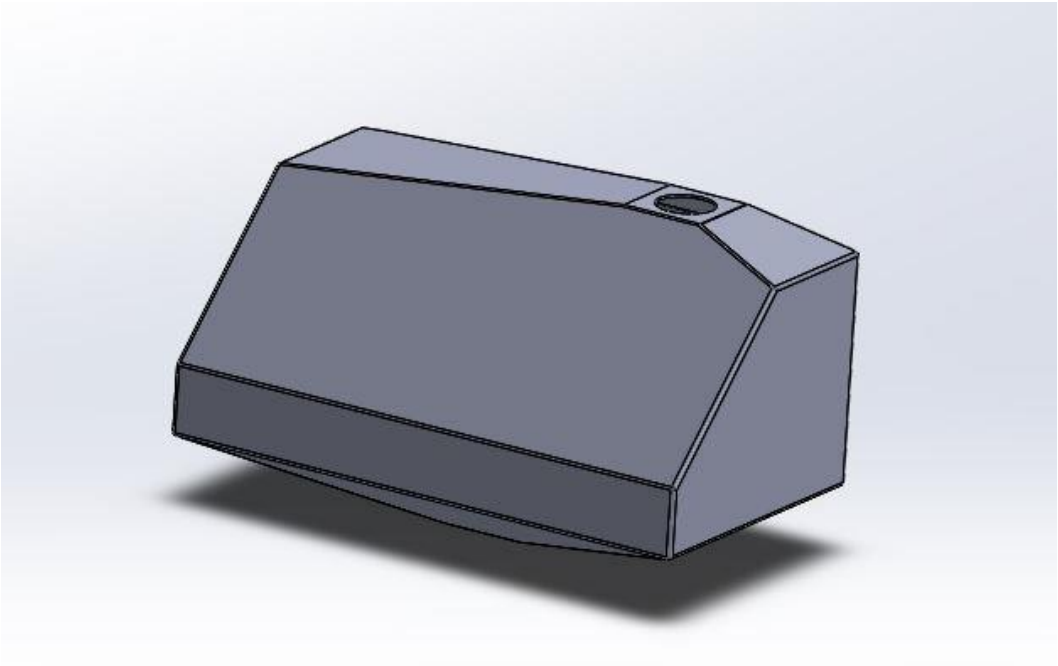

Figure 59: Current Design of Fuel Tank

The second biggest change to the fuel system is incorporating our first ever composite fuel tank shown in *Figure 59*. Fiberglass seems to be the ideal material for the tank so far as it is cheaper than carbon fiber and nonconductive. A composite fuel tank will be lighter than the previous fuel tanks which were made

from aluminum and if the proper epoxy resin or fuel tank liner is selected, the fuel tank won't degrade when exposed to E85. The fuel tank will have a volume of 2.2 gallons and will have to be E85 resistant.

Last year the car had a fuel tank with a 2 gallon capacity and we had enough fuel to last endurance. Our intake and exhaust should remain mostly the same and we haven't made any large changes to our tune so we are assuming a 2 gallon tank should hold enough fuel to get through endurance but we are adding the additional 0.2 gallons as a reserve just in case our tune has to be altered greatly due to the new location for the competition. The fuel tank will incorporate a tapered bottom to help direct fuel to one central portion within the tank, this should help the fuel pump have a constant feed of E85 through hard cornering. One major issue with the car at competition was that the fuel pump would run out of fuel in the tight hairpin corners where sloshing would direct the fuel in the tank away from the fuel pump pick up tube and would cause the engine to stall while racing. Flow simulations will have to be done to see how well the current fuel tank design maintains fuel in the central location where the fuel pick up tube is located. These simulations will be done in the Star CCM+ computational fluid dynamics program. Different angles for the bottom half of the fuel tank will be tested to find the optimal angle that will allow fuel to remain in the center of the tank even in a 1.2 g turn.

A second issue that was observed last year was that the aluminum would degrade as the E85 sat in the fuel tank. This would cause aluminum particles in the E85 to clog the fuel injectors. By choosing the correct fuel liner or epoxy resin, this problem could be remedied, and we would no longer have an issue with the fuel injectors clogging.

A third problem that was observed with last year's fuel tank was that air bubbles would form when the fuel tank was refueled. This was a problem when it came to the endurance because we are not allowed to shake the car after being refueled for endurance, so we were shorting ourselves of precious fuel for the final race. A solution to this problem is incorporated in the new fuel tank where the top of the tank is tapered to one central point where the fuel filler neck attaches to the tank. The thought behind this design is that as fuel is poured into the tank, the air should be allowed to escape up to the tapered end instead of

just meeting a flat surface and becoming trapped in corners of the fuel tank. This design will still need to be verified, either by experimentation using two small layups; one with a flat top and one with a tapered top and then pouring E85 into each and comparing which one has a lower fuel level, or finding a reliable source of literature to confirm this design idea.

Baffles have been considered for the fuel tank but it seems as though it would be difficult to incorporate the baffles into a mold of the fuel tank. Also since this is our first composite fuel tank, we would like to focus more on manufacturing a tank that does not leak and getting experience building composite fuel tanks for future years. One product that can eliminate the need for baffles is the Holley Hydramat, this is essentially a mat that is placed into the fuel tank and it absorbs any fuel that it contacts and contains the fuel within its reservoir. As the fuel is absorbed, any tiny pores that were open are closed by surface tension when there is very little fuel left in the tank. The fuel pump pick up is connected to the Hydramat so the fuel pump is constantly fed fuel even when the fuel tank is low on gas. The Hydramat would eliminate the need for baffles and would make the manufacturing of the fuel tank less difficult and time consuming. The Hydramat also acts like a 15 micro filter before the fuel pump, this would eliminate the need for a “pre filter” before our main fuel filter. We still need to confirm that the Hydramat is E85 compatible and we need to verify that the Hydramat is rules compliant, although so far the Hydramat does appear to be rules compliant and Holley states it is E85 compatible, as do multiple sources.

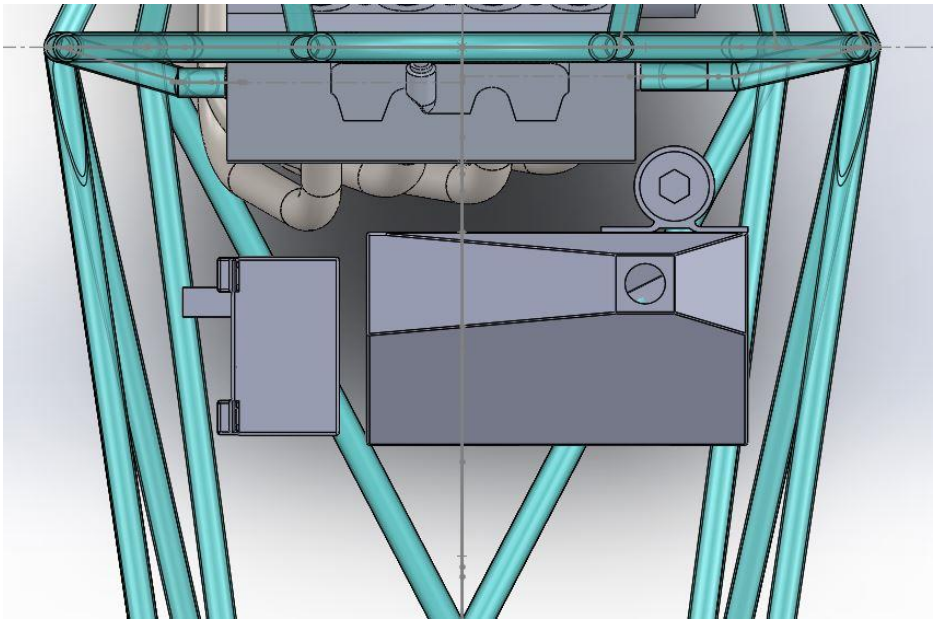

Figure 60: Fuel Tank Placement in Car From a Top Down View

The fuel tank will be placed as low as possible within the car to keep the center of gravity low and it will be behind the driver, on the left side of the car (looking from the rear end towards the front of the car) to keep it away from the exhaust which is located on the right side of the car and to make room for the battery. A top down view of the fuel tank's location is shown in *Figure 60.* A heat shield will be placed over the exhaust to prevent the fuel tank from getting too hot and the fuel tank will have thermal insulation around the sections exposed to radiating heat from the exhaust.

The tank will be manufactured in two halves, the top half and the bottom half. These two halves will be joined at the center. The two male molds will be made from MDF board which will be cut on the router in layer by layer sections and glued together to make the mold.

Other components of the fuel system include the external fuel pump which will be used again from last year, an E85 compatible plastic pick up tube inside the tank, steel braided hoses, a primary fuel filter, a fuel pressure regulator, the fuel rail which will get anodized as well, and the four fuel injectors. A drain

bolt will be required for the bottom of the tank as well. The fuel filler neck will be made from fiberglass as well, and will be made using a female mold which will also be made from MDF board.

The greatest cost for the fuel tank will be Holley Hydramat which will cost $155, the epoxy resin that seems to be E85 compatible costs $59 and we have the fiberglass that will be used for the tank and filler neck. The total estimated cost of the fuel tank is $220, this is accounting for a drain bolt along with the Hydramat and epoxy resin.

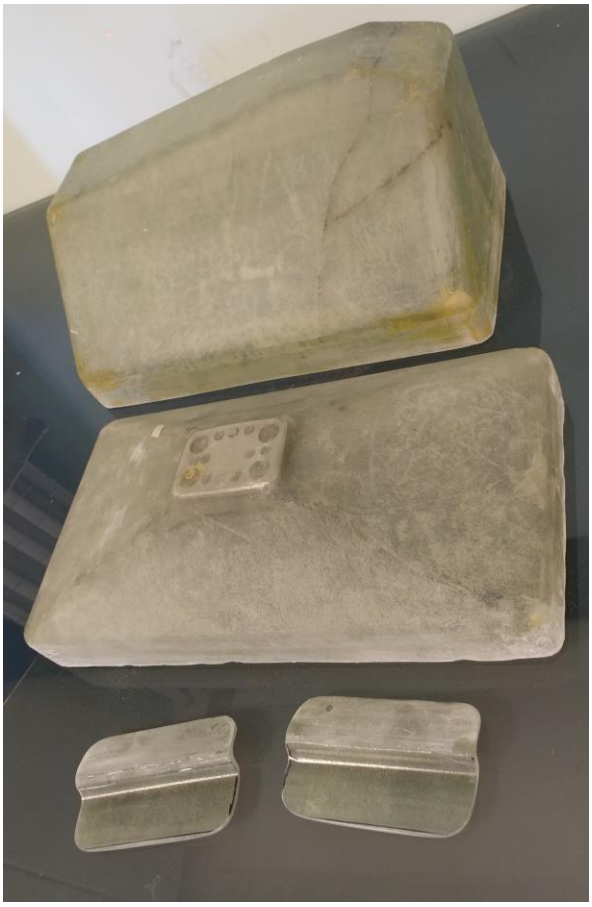

Figure 61: *Current State of Fuel Tank*

The majority of the fuel tank parts have been manufactured besides the filler neck. The two halves of the fuel tank were made using female MDF molds. The tabs were created by

making top and bottom MDF molds and laying up over the bottom mold and clamping the top mold over the bottom to compress the fourteen layers of fiberglass that the tabs are made from. The biggest challenge with making the fuel tank halves was releasing them from their molds and the free-coat tended to peel off with the part and remained on the parts. The fuel tank top stripped some of the MDF off the molds which was then stuck to the part. The main goal with the fuel tank right now is to assemble it and install it in the car before March 23rd. Currently all of the fuel tank pieces have been manufactured and will be assembled in a matter of days. Some repairs will be done to the top half of the fuel tank where a crack is believed to be located. Once the repair is finished the top half of the tank will be coated with an E85 compatible resin. The bottom portion of the fuel tank will have baffles added to it since the Holley Hydramat has not arrived yet. The baffles will help reduce sloshing in the fuel tank which was the intended purpose of the Hydramat. Once all four baffles are installed in the fuel tank bottom it can be coated in the E85 resistant resin and then the tank will be ready for assembly.

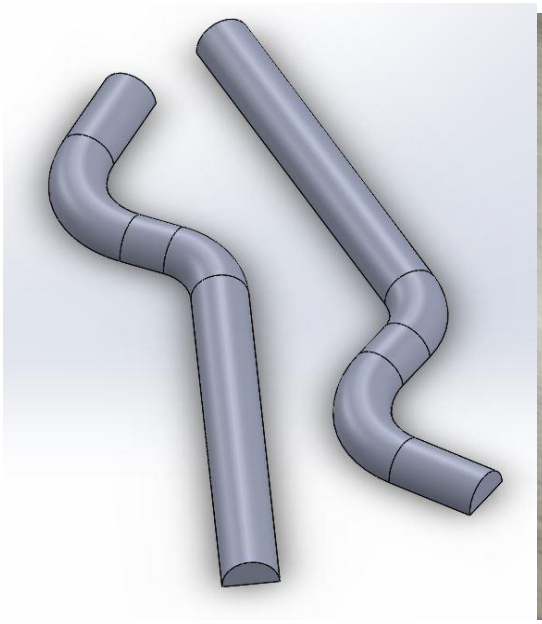

***Figure 62**: Two halves of the filler neck.*

***Figure 63**: Filler neck mold*

The filler neck has to be manufactured; a foam mold has been made for the filler neck. The foam mold was made in two halves on the Shop Bot, this is shown in ***Figure 62***. ***Figure 63*** shows the two halves combined to make the filler neck mold. The two halves were then bonded using hot glue and a wet layup will be done where fiberglass will be wrapped around the mold and then the mold will be put in a double sided bag to compress the fiberglass. Once the layup is finished, acetone will be poured into the filler neck to dissolve the foam mold. The mold is oversized so the fiberglass tube will have to be cut to size and then the filler neck cap and sight tube can be added. The filler neck cap threaded portion and cap from last year's car will be used, this portion will be cut from the old filler neck and bonded to the fiberglass filler neck. The filler neck will consist of five layers of fiberglass and will be bonded directly to the tank.

Cooling System

The purpose of the cooling system of an internal combustion engine (ICE) is to reject heat generated by the engine. A natural byproduct of the inefficiency of an ICE, is heat. As fuel is ignited inside the cylinder of an engine, heat is generated and subsequently transferred to the surrounding materials. A cooling system is designed to reject this heat to maintain a specified temperature. By maintaining a specified temperature, individual components of the engine are protected from overheating (melting or friction welding), the engine oil's lubricating properties are maintained, and the engine operates at its maximum efficiency.

The cooling system is comprised of six major components: a water jacket surrounding the engine block, a water pump, a thermostat, a circulating coolant within the closed system, a heat exchanger (radiator), and a fan. The water jacket is a series of passages surrounding the cylinders and cylinder head and promotes heat transfer between the engine and the coolant. The water pump on the CBR600RR engine is driven from the crankshaft, which means the rate of flow of

the coolant varies with engine RPM. The thermostat works in conjunction with the water pump to direct the flow of coolant, depending on the temperature of the coolant. When the thermostat is closed, the water pump circulates coolant within the water jacket only and does not allow coolant to flow to the radiator. This allows for the engine to reach operating temperature sooner than if the coolant was circulating through the radiator. On the CBR600RR, the thermostat is set to open at 185 °F. Once this temperature is reached, the coolant flows through the entire cooling system. The coolant in the system is water, rather than a more conventional ethylene glycol coolant; this is specified by FSAE rules.

The heat exchanger in the cooling system is in the form of a radiator. The radiator does most of the heat rejection in the system. It is made from aluminum, which has relatively high thermal conductivity. Higher thermal conductivity increases the rate of heat transfer to the surroundings in comparison to a material with a lower conductivity. The radiator has fluid passages, called cores, that allow the coolant to travel from one end of the radiator to the other. Depending on the size of the radiator, there can be anywhere from 10 to 100 cores in a single radiator. Attached to the cores are thin aluminum fins that increase the surface area of the cores, which also increases the amount of heat rejected from the system. The radiator is connected to the engine via coolant hoses in order to circulate the coolant through the system. A fan is incorporated on the backside of the radiator so that heat can be removed from the system effectively, even when the vehicle is stationary.

A difficult aspect of designing the cooling system is determining how much heat needs to be removed from the system. There are many variables that affect both the amount of heat generated by the engine, and how effective the cooling system is at removing that heat. Some of the variables that must be considered include ambient temperature, altitude, mass flow rate of the

air entering the radiator (a function of temperature, density, area, and velocity), the mass flow rate of coolant circulating in the system, the overall size of the radiator (including the number of cores and the density of the fins), and the amount of heat generated by the engine that is transferred to the cooling system.

Since determining the amount of heat being transferred to the cooling is such a difficult task, we rely on a general rule of thumb that the heat produced by the engine is equal to that of the power output. The amount of heat produced is split between the exhaust and the cooling system at roughly 50% each. That means if an engine produces 50kW of power, approximately 25kW are transferred to the cooling system.

In order to account for all variables when designing the cooling system, an excel spreadsheet was created to determine the amount of heat transfer of which the radiator was capable. The spreadsheet included mass flow rates of the water pump that were conducted by the 2019 FSAE team. By incorporating this data, the spreadsheet seen in Appendix 1, calculated the heat transfer of the radiator and allows for all input variables to be changed. The spreadsheet includes calculations necessary for determining convective heat transfer coefficients of the radiator cores and fins, such as Reynolds numbers, Nusselt numbers, fin efficiency, effective area of fins, and friction factors. These calculations were used to find an overall heat transfer coefficient, UA. The log mean temperature difference (LMTD) was also calculated using fluid properties at the input values. Additionally, since most commercially-available radiators utilize a crossflow pattern, rather than the traditional counter flow pattern in heat exchangers, a correction factor, F, was also necessary for accurate calculations of heat transfer. The value of F was obtained from *A Heat Transfer Textbook*[123]. The total heat transfer, Q, was calculated using the following equation:

$$Q=UA(LMTD)F$$

A contributing factor to how effective the radiator is at rejecting heat from the system is the design of the sidepod in which the radiator is housed. In order to optimize the transfer of heat from the radiator to the incoming air, a pressure differential must be generated in order to prevent stagnation at the sidepod inlet. To accomplish this, the area of the sidepod inlet needs to be less than the area of the radiator, and less than the exit of the sidepod. The inlet needs to be between 40% and 60% the size of the radiator to optimize heat transfer. The current design of the sidepod can be seen in Figure 64

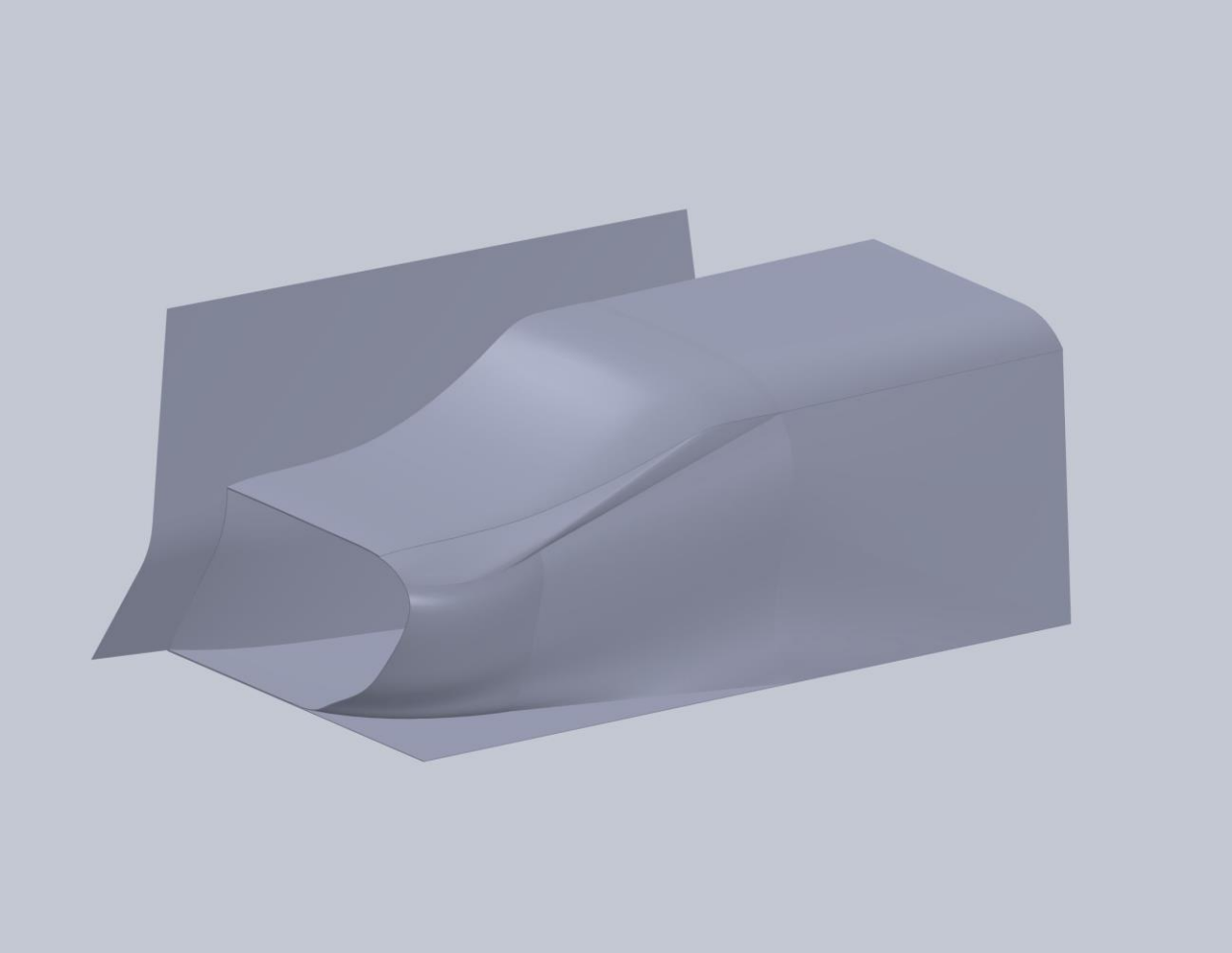

Figure 64: *Current design of sidepod which contains radiator.*

The overall size of the sidepod should also be taken into consideration in order to reduce drag. To accomplish a reduced cross-sectional area, the radiator can be tilted at an angle, rather than perpendicular to the flow of the incoming air. A downside to a tilted radiator is the potential for the flow of air to stall behind the fins due to an extreme angle of attack. The current design of the sidepod includes turning vanes just before the radiator to condition the flow, such that the angle of attack is as close to zero as possible. The turning vanes will be made from carbon fiber and attached as a shroud on the inlet of the sidepod. There will also be a mesh screen placed just in front of the radiator. The purpose of the mesh is twofold. First, the mesh will protect the fins of the radiator from debris thrown into the sidepod from the tires. The mesh will also generate turbulence (increase the Reynolds number) in the flow of air as it contacts the radiator. As the Reynolds number increases, the Nusselt number also increases. By increasing the Nusselt number, the convective heat transfer coefficient is increased, thus leading to an increase in overall heat transfer.

Based on the calculations provided by the spreadsheet and the previous year's testing, an existing Mishimoto radiator has been chosen as a suitable component for this year's car. The radiator measures 12"X8"X2" and has 20 cores with 200 fins per row and is seen in Figure 63

Figure 65: *Mishimoto radiator selected for use on the 2019-2020 FASE car. (Mishimoto.com)*

The radiator will be placed at a 45° angle to the incoming flow, and will have five turning vanes to condition the flow before the radiator, as seen in Figure 65.

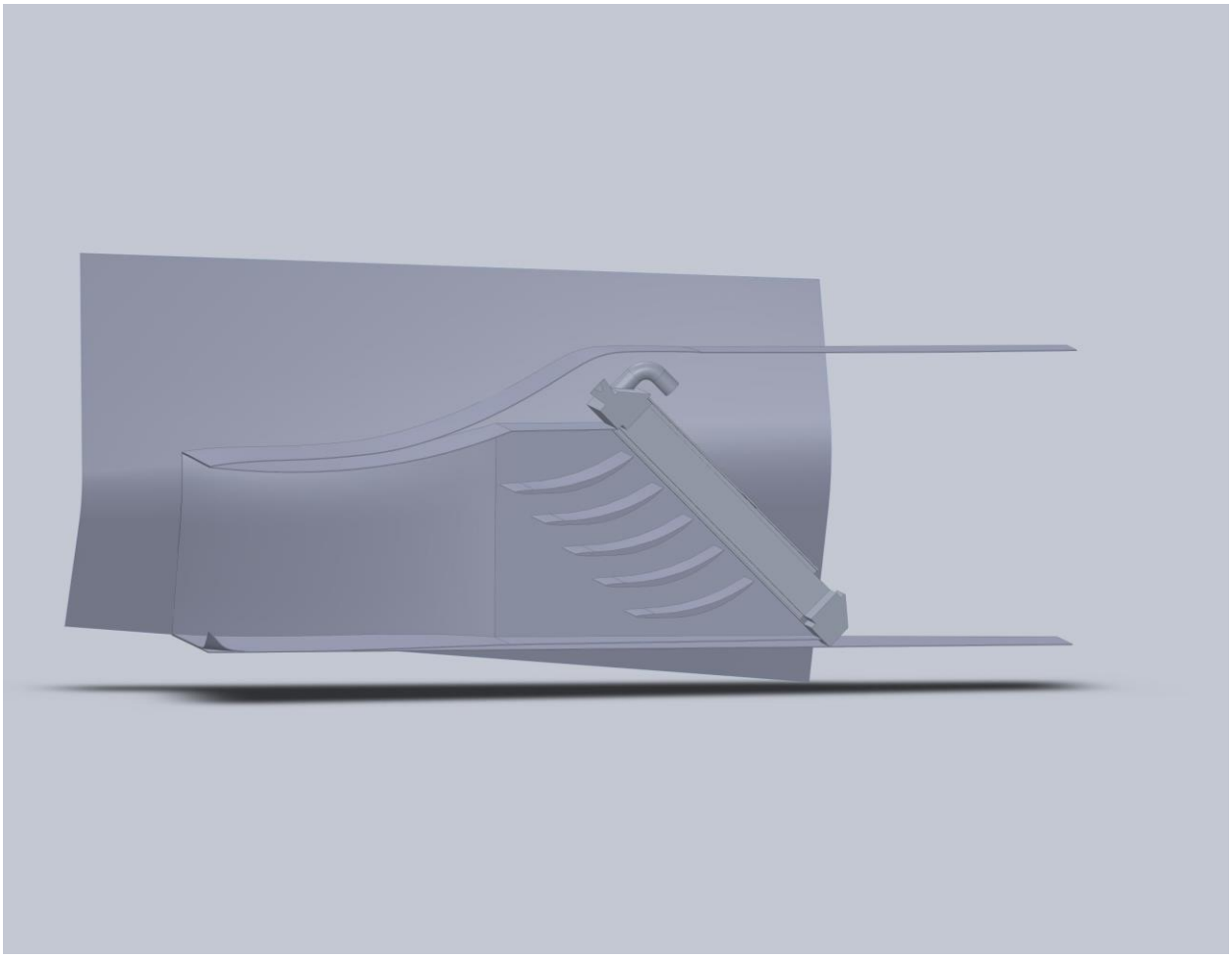

Figure 66: *A cut view of the sidepod and radiator to show the turning vanes contained within the radiator shroud.*

In addition to the calculations conducted within the spreadsheet, CFD models will be performed using STAR CCM+ to verify the calculations. The CFD models can also provide feedback as to what changes will maximize the performance of the radiator and minimize drag. Additionally, the CFD results will confirm the success (or failure) of the turning vane concept. If the CFD results indicate that the vanes are not effective at conditioning the flow into the radiator, the vanes will not be incorporated in the final design of the car.

Testing

In order to verify the accuracy of the calculations provided by the spreadsheet, temperatures and airspeeds were recorded during several dyno runs on last year's car. The temperatures were recorded using four Type K thermocouples and a data logging software. The four temperatures measured were radiator inlet and outlet temperatures, incoming air temperature, and outlet temperature on the backside of the radiator. To measure the velocity of the air coming into the sidepod, a pitot-static tube was used in conjunction with a dynamic pressure gauge. Atmospheric pressure and temperature were used with the Ideal Gas Law to calculate the density of the air, which was then used to determine the velocity of the incoming air. Inputting these variables into the spreadsheet produced values of heat transfer that were between 15 and 18 percent different than the theoretical values. Several factors can be attributed to the error in these calculations. First, the mass flow rate of the coolant is not constant during a dyno run. The calculations were made using the mass flow rate at an average engine RPM of 8000. Additionally, minor losses due to the complex geometry of the radiator were not accounted for, which has an effect on the mass flow rate of the coolant. Another source of error in the calculations is how the temperatures of the coolant were measured. Due to the nature of the Type K thermocouples, the temperature of the coolant was measured indirectly at the surface of the radiator inlet and outlet, rather than the temperature of the coolant itself. The thermal resistance of the tubing at which the temperatures were measured was not accounted for. Even with this relatively large amount of error between theoretical values and experimental values, the calculations show that the 12X8X2" radiator will be sufficient at cooling the engine during the most demanding events at the FSAE competition.

In addition to the original design of the cooling system, a 10 inch diameter fan was selected to aid cooling at low speeds, and a fan shroud was designed to maximize fan efficiency.

The 10 inch fan has a maximum flow rating of 1081 cubic feet per minute. With the fan providing this flow rate, the radiator is capable of rejecting 13,000 Watts of energy from the system at a standstill with 80° F ambient temperatures. This amount of cooling equates to the car travelling at a speed of 22 miles per hour without a fan.

Designing the fan shroud presented several challenges in terms of packaging due to the size of the fan in relation to the radiator. Since the radiator has a width of 8 inches, and the fan a diameter of 10 inches, the fan could not be mounted directly to the radiator without restricting a significant amount of flow. To combat this issue, a gently tapered shroud was designed to optimize the flow of air through the radiator. Additionally, due to the unique location of the radiator exit, the shroud also incorporated an offset to accommodate the radiator's plumbing. The final shroud design is seen in Figure 67

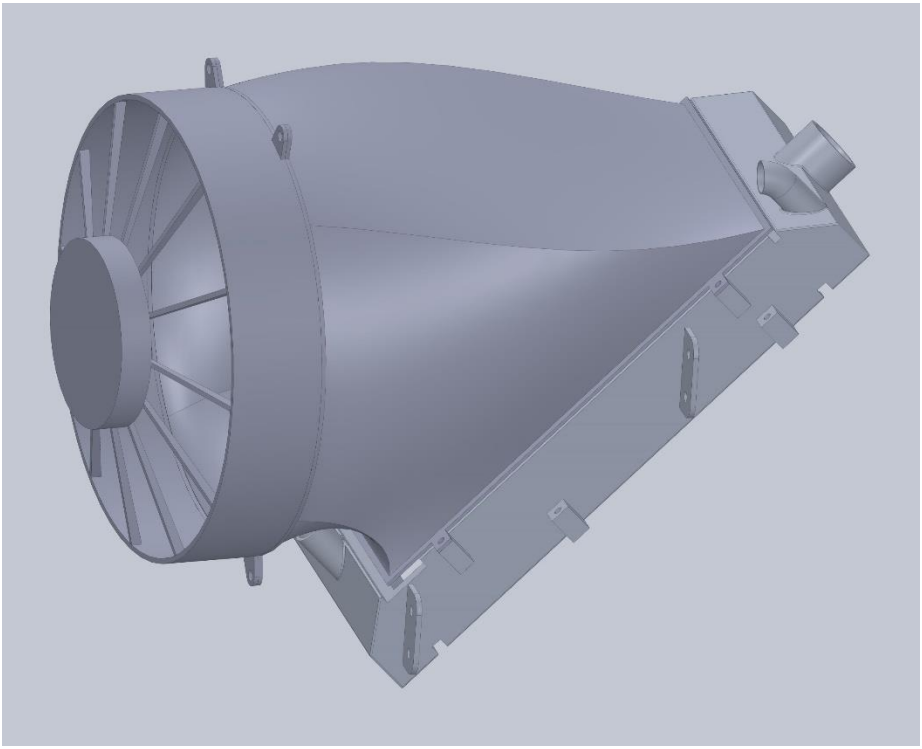

Figure 67: *Solidworks model of final fan shroud design attached to radiator.*

Testing

In order to verify that the radiator calculations were accurate, and to ensure the selected radiator and fan combination was sufficient, data was collected during a day of test driving. The selected cooling components were fitted to the car with the fan mounted directly to the rear of the radiator. Testing was conducted in a large parking lot that provided ample space to drive the car in a manner that simulated the most demanding aspects of the FSAE competition. Data collected during the test showed the cooling capabilities of the system were more than sufficient to keep the engine within the manufacturers recommended operating temperature.

CFD analysis was performed using Solidworks Flow Simulation to verify the concept of the turning vanes in the inlet ducting. The goal of the vanes was to turn the flow of air parallel to the direction of the fins. Turning the flow will reduce the likelihood of a stalling effect behind the fins which would reduce the effectiveness of the radiator. The flow trajectory lines seen in Figure 68 verify that the direction of flow is turned to nearly 45° which the radiator is also angled.

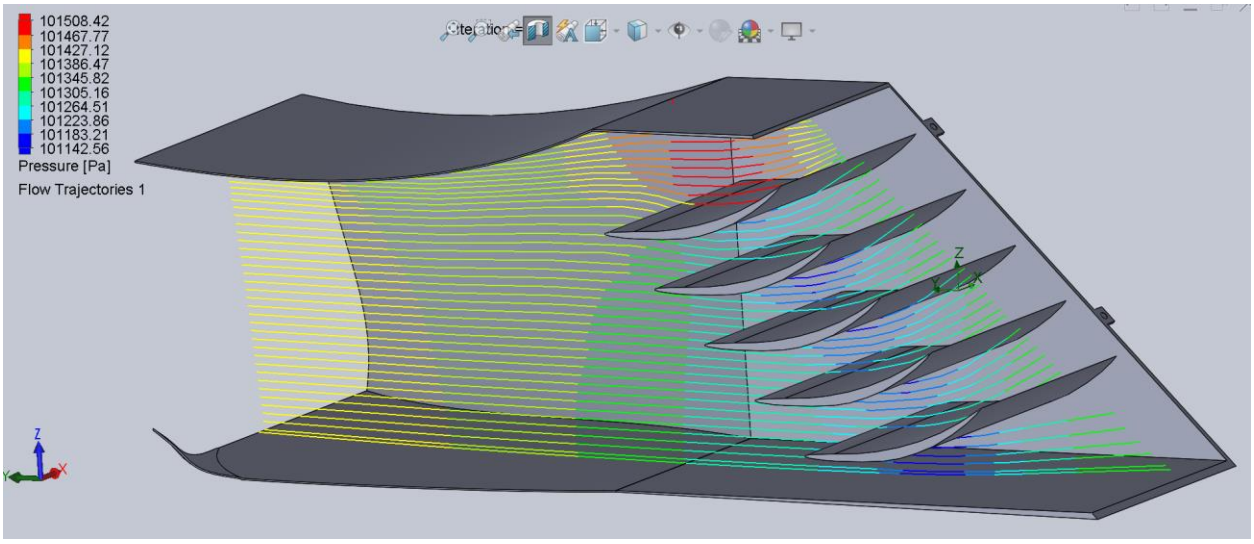

Figure 68: *Flow trajectories provided by Solidworks Flow Simulation show the flow of air entering the radiator parallel to the angle of the fins.*

The coolant hose routing has been finalized, and larger hoses will be purchased to make use of the increased size of the radiator plumbing. The routing can be seen in Figure 69

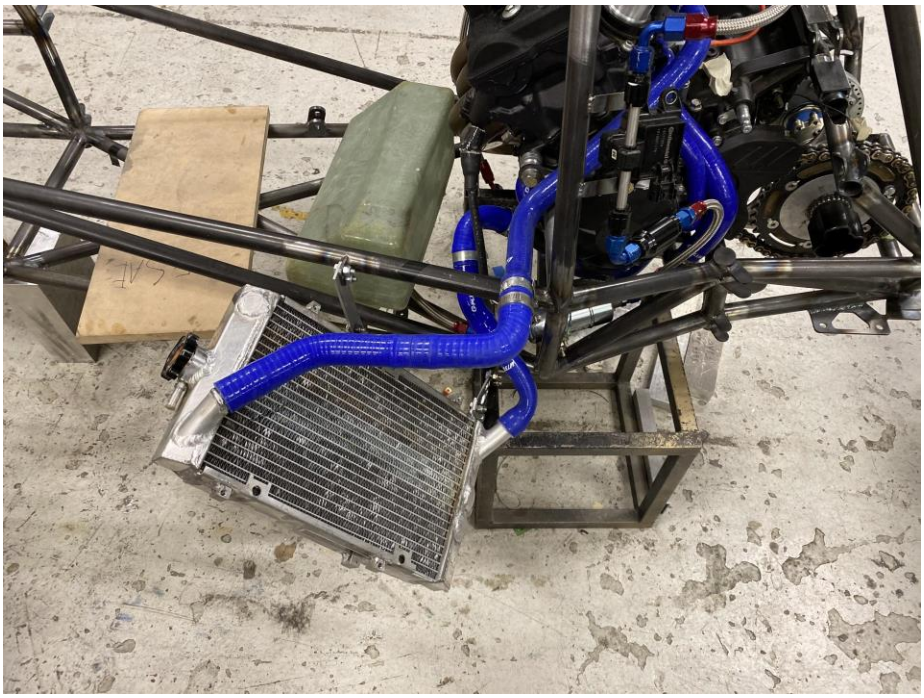

Figure 69: *Temporary coolant hoses used to determine hose routing.*

The two-piece carbon fiber fan shroud has been made. The shroud was made in two pieces due to the complex shape needed for packaging purposes. A joggle was used to overlap a section of the shroud to provide enough surface area to bond the halves together with composite epoxy. After the shroud is bonded, it will be trimmed to final dimensions and have the fan and radiator attached. The carbon fiber fan shroud can be seen in Figure 70

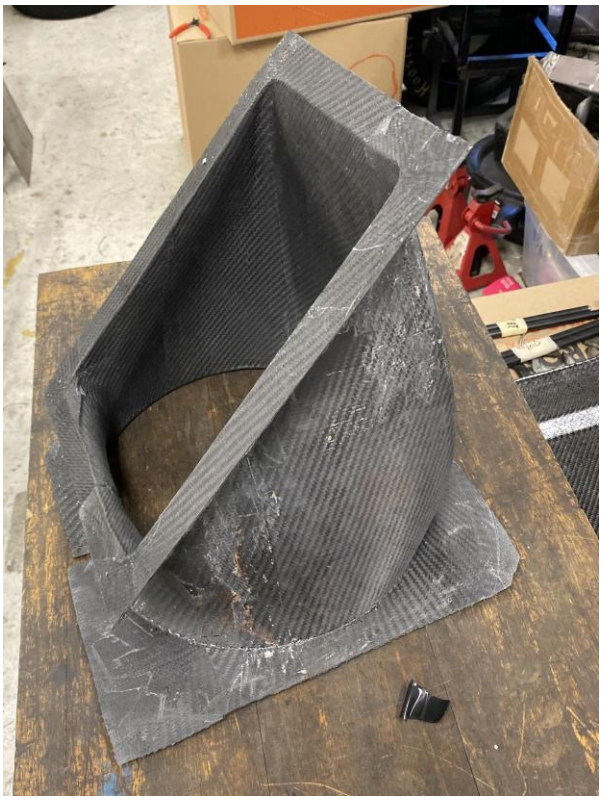

Figure 70: *Carbon fiber fan shroud.*

Differential Mounts

The differential and drivetrain will use the same chain system model used on last year's vehicle. This year's differential mounts will use an eccentric bearing design that will keep tension on the sprocket, and the differential and drive train will use a dual sprocket design, one

mounted onto the engine output shaft and another sprocket mounted onto the rear differential. The redesign of the car allowed for the differential mounts to also be redesigned. Using the following equations, the radial forces exerted by the engine and onto the rear sprocket were calculated.

$$F_t = \frac{\dot{W}(33000)}{v_t}$$

$$F_r = F_t \tan(\emptyset)$$

Where ‘d’ is the gear pitch diameter, ‘n’ is the RPM of the shaft, Ẇ is the power transmitted in horsepower, and θ is the pressure angle between the contact of the chain, and rear sprocket. The radial force was then determined, and a new slimmer bearing was chosen, which was half the width of the previous bearing while still being able to maintain a Safety Factor > 2. The slimmer bearing allowed the differential mount to also be slimmed down, and after FEA analysis, the mount could be manufactured using 6061 T6 Aluminum, with a Safety Factor of 3.9. In addition, the weight of the differential mounts has been reduced by 27%. The radial loads and Safety Factor from the FEA analysis can be seen in figures 71 and 72

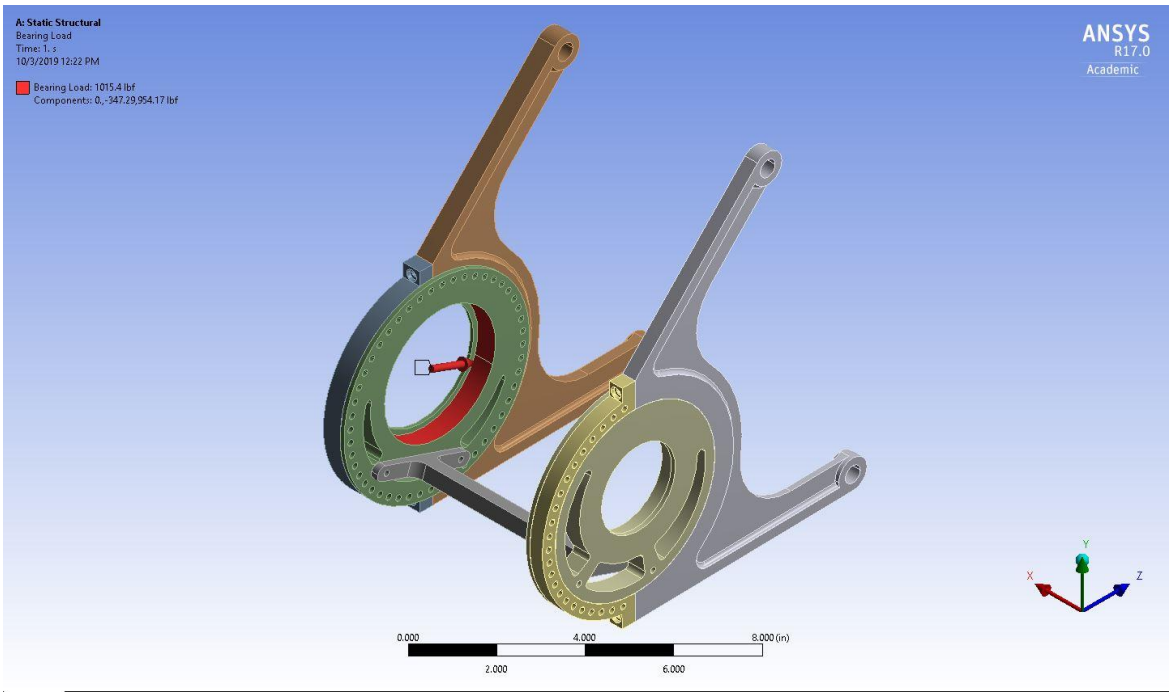

Figure 71: *Radial Loads produced by the engine output.*

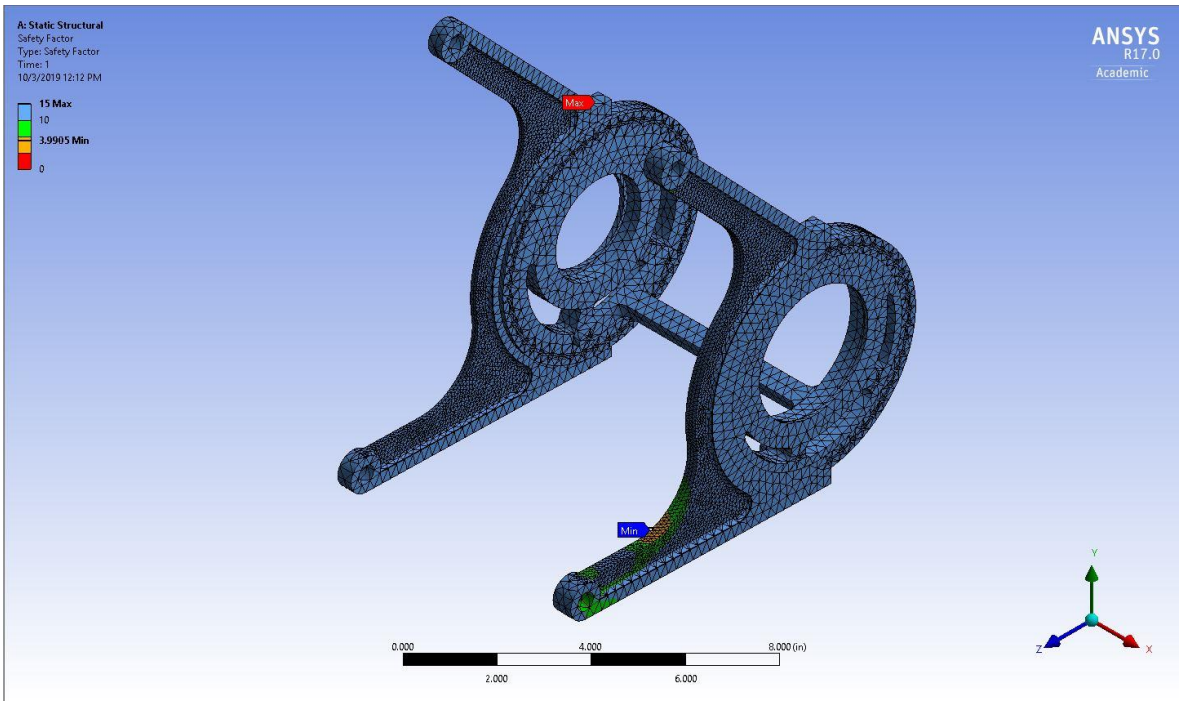

Figure 72: *Safety Factor FEA Analysis*

Final Drive Ratio

Due to the change in tire size for this year's design, the performance of the car would be significantly affected if the Final Drive Ratio was also not adjusted. Simply, a smaller tire radius would allow for more vehicle acceleration but would have an inverse effect on the vehicle speed. This in itself would be a good thing, to have more acceleration; however there is a limit to how much force can be transmitted onto the tires. Too much force, and the force would overcome the traction limitation between the contact of the road and the tire, thus the tire would spin out providing no forward acceleration. Decreasing the Final Drive Ratio would decrease the forward acceleration, and increase the vehicle speed. Thus the primary goal for this is to find the optimal balance between acceleration and speed and adjusting the Final Drive Ratio to meet that balance. The forward force of the car can be determined using the following equation.

$$F_x = \frac{T_e N_{tf} \eta_{tf}}{r} - \left\{(I_e + I_t){N_{tf}}^2 + I_d {N_f}^2 + I_w\right\}\frac{a_x}{r^2}$$

Where, T_e, is the torque of the engine, 'N' are the gear ratios of the transmission, final drive ratio, or both, 'I' are the inertial moments of the rotating assemblies, and 'r' is the radius of the tire. Adjusting the Final Drive Ratio, the 'N' value, will either increase or decrease the forward force of the car, and the relationship between each gear, the Final Drive, the traction limitation, and the force and speed can be observed in figure 73. The final piece of the puzzle is to determine the current traction limitation of the car based on the final weight of the car, the coefficient of friction, and the downward force provided by the Aero Package assemblies. Once those values have been determined, than the Final Drive Ratio can be adjusted so that most of the

force curve of the vehicle falls below the traction limitation while still providing adequate amount of acceleration as noted in figure 53.

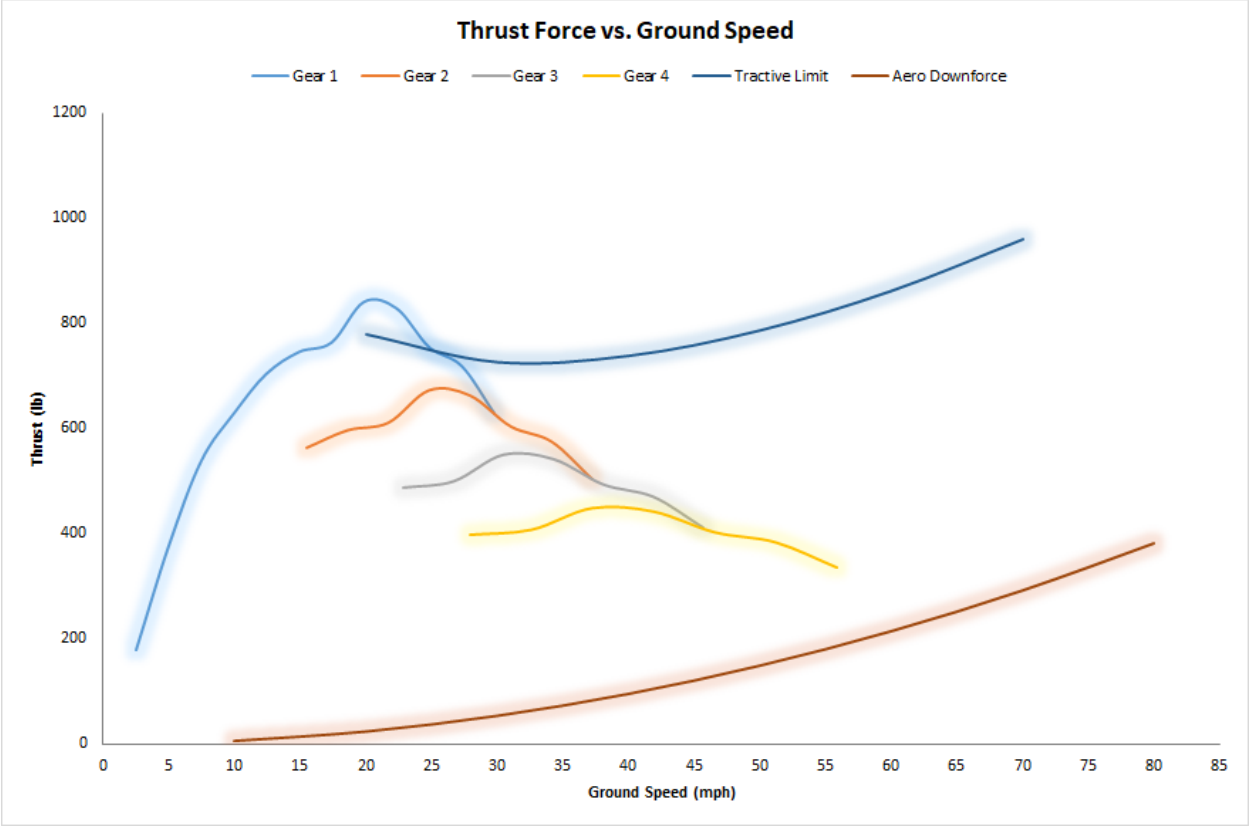

Figure 73: *Ground Speed Vs Thrust and Traction Limitation*

Composites/Aero

Since the start of the winter break all of aero package molds were made and prepared a week into break. After the molds were ready for layup work began on body molds. CAM for body molds, nosecone, and side pods were completed before the start of the new year along with helping rover with molds. By the start of spring semester all molds are done. Most of the challenges have come from others breaking the shopbot and me having to figure out what to do to fix it. MDF is not an ideal mold material that has failed us many times. The prep stage takes so much time that it is almost easy to beg every company to machine the molds for us. Tolerance is low and if the mold falls 2 feet it breaks. It soaks up so much resin if it is not fully sealed and polyurethane does not like to work with industry grade materials.

Figure 74: *Shopbot Body Side panel*

Figure 75: *Nosecone*

Figure 76: *Both Bodies, Fuel Tank, Battery box, Dash, Main Wing*

Conclusion

The 2019-2020 team is most of the way through manufacturing and up until the COVID-19 worldwide crisis was on schedule for the fastest and most successful FSAE car that this university has ever built. The major subsystems of engine and driver interface still have parts that needed to be manufactured and placed in the car for first drive. All major suspension parts are manufactured and will be attached to the car as soon as possible. After the university shutdown the team continued to work as hard as possible in a teammates garage before the news came that the California SAE competition had been cancelled. This team worked incredibly hard and hit all technical goals that had been outlined at the start of the year. Unfortunately, the team cannot meet during COVID and with the competition cancelled the car will remain unfinished until it is safe to resume having team meetings.

References

1. Speer, Jeff. “Circuit Racing Tires.” *Hoosier Racing Tires*, www.hoosiertire.com/tires/circuit/spec/#more.
2. Miliken, Doug. “Tire Test Data Round 8.” *FSAE TTC*, 21 Oct. 2018.
3. Lienhard, John H., and John H. Lienhard. *A Heat Transfer Textbook*. 4th ed., 2018.
4. McBeath, Simon. *Competition Car Aerodynamics: A Practical Handbook*. Veloce Publishing Limited, 2017.
5. *Yamaha YFM660 Raptor Aluminum Radiator, 2001-2005*. https://www.mishimoto.com/yamaha-yfm660-raptor-aluminum-radiator-01-05.html. Accessed 8 Oct. 2019.
6. Puhn, Fred. *How to Make Your Car Handle*. H.P. Books, 1986.
7. Dietzsch, Curtis. “Finding Your Center – Finding Your Front and Rear Roll Center.” *OneDirt*, 17 May 2018, www.onedirt.com/tech/chassis-suspension/finding-your-center-finding-your-front-and-rear-roll-center/.
8. Flickinger, Evan. “DESIGN AND ANASLYSIS OF FORMULA SAE CAR SUSPENSION MEMBERS.” *Scholar Works, California State University* , 2014, scholarworks.csun.edu/bitstream/handle/10211.3/123383/Flickinger-Evan-thesis-2014.pdf?sequence=1.
9. Wardana, Muhammad & Praptijanto, Achmad & Kaleg, Sunarto. (2015). Measuring Geometric and Kinematic Properties to Design Steering Axis to Angle Turn of The Electric Golf Car. Energy Procedia. 68. 463-470. 10.1016/j.egypro.2015.03.278.
10. Gaffney, Edmund F., and Anthony R. Salinas. “Introduction to Formula SAE® Suspension and Frame Design.” *SAE Transactions*, vol. 106, 1997, pp. 92–102. *JSTOR*, www.jstor.org/stable/44722738.
11. Seas. “Wheelbase.” *Wheel Base*, www.formula1-dictionary.net/wheel_base.html.
12. Gillespie, Thomas D. *Fundamentals of Vehicle Dynamics*. Society of Automotive Engineers, 1994.
13. Juvinall, Robert C., and Kurt M. Marshek. *Juvinall's Fundamentals of Machine Component Design*. Wiley, 2017.
14. Kazprzak, J. “Understanding Your Dampers.” Kaz Technologies p10.
15. Fox, S. “Cockpit Control Forces.” Formula SAE, 2010.